NEVADA DOT

SAFE AND CONNECTED

Nevada Department of Transportation

Report No. 296-22-803

Developing Quality-Controlled Datasets and Methods to Assess the Impact of Rain on Snow Events on Nevada Highways

June 2024

Disclaimer

This work was sponsored by the Nevada Department of Transportation. The contents of this report reflect the views of the authors, who are responsible for the facts and the accuracy of the data presented herein. The contents do not necessarily reflect the official views or policies of the State of Nevada at the time of publication. This report does not constitute a standard, specification, or regulation.

TECHNICAL REPORT DOCUMENTATION PAGE

1. Report No. 296-22-803	2. Government Accession No.	3. Recipient's Catalog No.
4. Title and Subtitle Developing Quality-Controlled Datasets and Methods to Assess the Impact of Rain on Snow Events on Nevada Highways		5. Report Date July 2024 6. Performing Organization Code N/A
7. Author(s) Anne Heggli, Brennan Bean, Benjamin Hatchett, Emma Anderson, Marc Maguire, Fray Pozo-Lora, Jon Meyer		8. Performing Organization Report No. Click or tap here to enter text.
9. Performing Organization Name and Address Desert Research Institute (DRI) 2215 Raggio Pkwy, Reno, NV 89512		10. Work Unit No. 11. Contract or Grant No. P296-22-803
12. Sponsoring Agency Name and Address Nevada Department of Transportation 1263 South Stewart Street Carson City, NV 89712		13. Type of Report and Period Covered Final Report 06/27/2022 to 06/30/2024 14. Sponsoring Agency Code
15. Supplementary Notes Click or tap here to enter text.		

16. Abstract

The most damaging effects of rain-on-snow (ROS) events are often the result of excess water flows disrupting downstream infrastructure. While rain on snow events have been well studied in previous literature, there exists little research that quantifies the impact of ROS events on infrastructure. This report outlines efforts to explore the influence of ROS events on roadway infrastructure in the state of Nevada. In so doing, we create a Snowpack Runoff Decision Support System that is supported by rigorously cleaned measurements of hourly snowpack in the state of Nevada, with a focus on the Upper Carson River Watershed. Further, we quantify the excess stream surge associated with ROS events through the development of a new stream surge database that links over 7,000 recorded stream surges to the snow and weather conditions that preceded the surge at upstream SNOTEL stations. This database results in a recommendation to adjust NDOT flow calculations by 10-20% in locations of the state where ROS is expected to be an issue, and sample designs are provided to illustrate the implications for NDOT in implementing such an adjustment. Taken together the deliverables described in this report provide NDOT with a suite of data and tools to help improve infrastructure design to handle future extreme ROS events.

17. Key Words Rain-on-snow, snowpack, flooding, decision support	18. Distribution Statement No restrictions. This document is available through the: National Technical Information Services Springfield, VA 22161 www.ntis.gov

19. Security Classif (of this report) Unclassified	20. Security Classif (of this page) Unclassified	21. No. of Pages 55	22. Price n/a

Developing Quality-Controlled Datasets and Methods to Assess the Impact of Rain on Snow Events on Nevada Highways

(PI) Anne Heggli[1], (Co-PI) Brennan Bean, Ph.D[2], (Former PI) Benjamin Hatchett, Ph.D[1], (Student) Emma Anderson[2], (Co-PI) Marc Maguire, Ph.D[3], (Post-Doc) Fray Pozo-Lora, Ph.D[3], (Co-PI) Jon Meyer, Ph.D[4]

[1] Atmospheric Science, Desert Research Institute, Reno, NV
[2] Department of Mathematics and Statistics, Utah State University, Logan, UT
[3] Durham School of Architectural Engineering and Construction, University of Nebraska - Lincoln, Omaha, NE
[4] Utah Climate Center, Utah State University, Logan, UT

Abstract

The most damaging effects of rain-on-snow (ROS) events are often the result of excess water flows disrupting downstream infrastructure. While rain on snow events have been well studied in previous literature, there exists little research that quantifies the impact of ROS events on infrastructure. This report outlines efforts to explore the influence of ROS events on roadway infrastructure in the state of Nevada. In so doing, we create a Snowpack Runoff Decision Support System that is supported by rigorously cleaned measurements of hourly snowpack in the state of Nevada, with a focus on the Upper Carson River Watershed. Further, we quantify the excess stream surge associated with ROS events through the development of a new stream surge database that links over 7,000 recorded stream surges to the snow and weather conditions that preceded the surge at upstream SNOTEL stations. This database results in a recommendation to adjust NDOT flow calculations by 10-20% in locations of the state where ROS is expected to be an issue, and sample designs are provided to illustrate the implications for NDOT in implementing such an adjustment. Taken together the deliverables described in this report provide NDOT with a suite of data and tools to help improve infrastructure design to handle future extreme ROS events.

Background

Major winter floods and extreme runoff in Nevada often result from mid-winter rain-on-snow (ROS) events. In the Sierra Nevada, ROS events can produce 50-80% higher peak flows than spring snowmelt since rainfall and snowmelt together can produce greater floods than either just rainfall or snowmelt alone(Kattlemann, 1997). Furthermore, recent research suggests ROS-prone regions, such as the Sierra Nevada, are approaching a period of "peak ROS" as snow-dominated regions are expected to experience more frequent ROS before a warming-induced decline in snowpack volumes (Siirila-Woodburn et al., 2021).

Despite growing research on the hydrological impact of ROS events in the Sierra Nevada, there is little research on the direct impact of ROS or other snowmelt flood events on Nevada's road infrastructure elsewhere in the state. Nevada's most notable recent floods occurred in February 1986, January 1997, January 2006, and January and February 2017, however; snowmelt-induced slope failures, such as on Slide Mountain, also pose hazards to downstream roads and communities (Figure 1). Whenever flooding or extreme runoff damages highways or related infrastructure, the economic impacts can exceed millions of dollars for repairs and travel delay costs. Many roads in Nevada are located in areas susceptible to winter and/or spring flooding and require mitigation strategies such as the Carson Wash (Figure 1) to minimize impacts. The 1997 New Year's flood resulted in around $1 billion worth of damage in the Reno-Sparks region (Rhoades et al., 2023). In January 2017, areas between McCarran Boulevard and Hidden Valley were submerged from a rain-on-snow flood event in the Reno-Sparks area. Industrial area and land south of Interstate 80 also flooded as multiple inches of rainfall fell in the foothills and throughout the Sierra Nevada, west of Interstate 580 and U.S. 395. Several years later, extreme rainfall in early December 2021 caused erosion and culvert failure on NV-431 (Mt. Rose Highway; an average of 8,000 vehicles/day; Figure 1) and resulted in a multi-day closure of the road and simultaneous closure of the Mt. Rose Ski Resort as customers could not access the resort.

Figure 1: **Examples of cool season flood impacts on Nevada roads.** Clockwise from left: Snowmelt or extreme rainfall on Slide Mountain can produce debris flows that impact NV-580; Flood deposits on NV-580 following the May 1983 flood; The Carson City Wash mitigates flood impacts; NDOT workers repair a damaged culvert on NV-431; Erosion from extreme runoff damaged NV-431.

The ROS flooding problem presents an opportunity to identify high-risk weather and antecedent snowpack conditions . This opportunity provides additional lead time when staffing or preparing mitigation effort (e.g., staging equipment or cleaning culverts and drainage structures) for forecasted high-impact events. It can also improve the understanding of ROS runoff potential that could be integrated into transportation infrastructure design. While there is documented information about the meteorological factors that create

ROS flooding, the role of the snowpack is less well-understood. Therefore, this project has four principle objectives:

1. Identify regions in Nevada most susceptible to mid-winter ROS flooding.
2. Apply the Snowpack Runoff Decision Support System framework developed by Heggli et al. (2022) to Nevada and California snow monitoring stations with an operational decision-making focus on the Upper Carson watershed.
3. Quantify the expected surcharge in flow due to ROS using a ROS dataset from across the western states.
4. Provide guidance to NDOT regarding how to account for excess flows due to ROS in culvert design.

It is well documented that the far western region of Nevada experiences high-impact ROS events; however, there is little evidence of hydrologically-impactful ROS events in the far eastern regions. There is a greater uncertainty about where across the state the impacts of ROS events are meaningful for transportation. The first product aims to identify regions most susceptible to ROS runoff by looking at SNOTEL soil moisture to identify snowpack runoff and USGS streamflow to validate the ROS runoff response. This provides a first-level understanding of regions that have experienced impactful ROS events.

The Snowpack Runoff Decision Support System (SR-DSS) aims *to improve forecast confidence of hydrometeorological outcomes to help protect life and property while also optimizing increasingly scarce water resources* (Hatchett et al., 2020; Uccellini and Ten Hoeve, 2019). There is an outstanding need to communicate real-time changes in the snowpack during ROS events to forecasters and water managers across the Western U.S. (McCabe et al., 2007; Heggli et al., 2022). To address this need, we have developed a framework for SR-DSS, which is currently designed to provide situational awareness to communicate real-time changes in the snowpack at hourly timescales.

Further, our exploration of ROS events across the western states allows us to better quantify the potential gap between the flows currently being estimated by NDOT's implementation HEC-HMS using Atlas 14. We then pair the results of this exploration with some real design examples to demonstrate the implications of incorporating our results into culvert design in the state of Nevada.

The remainder of the report is organized into two super-sections, namely

- Nevada Decision Support,
- Western State Explorations,

Each super-section contains a Research Approach and Findings and Applications Section. The report also includes a section illustrating the implications of adopting a ROS surcharge factor on several real culvert design examples from historical NDOT projects. The report then concludes with a summary of findings across super sections. Taken together, the deliverables described in this report provide the most comprehensive exploration of the influence of ROS events on roadway infrastructure to date.

Research Approach - Nevada Decision Support

Study Area

The data collected are applied to the entire state of Nevada with a regional study that focuses on the Upper Carson River watershed. The Upper Carson is a sub-basin within the Carson River watershed. The Carson River watershed has two main forks feeding the Carson River and runs a total of 296 km (USGS, 2022). The East Fork (119 km) begins on the northern slopes of Sonora Peak at an elevation of 3,200 m while the West Fork (64 km) begins near Lost Lakes at 2,700 m. Both forks flow from California eastward and join near Genoa, Nevada before flowing through Carson City, NV to the Carson Sink at an elevation of approximately 1,180 m. The Upper Carson is 2,482 km^2 in area and has 12 NRCS SNOw TELemetry (SNOTEL) stations (see description in "Datasets" section) that are representative of the watershed. Six of those are within the watershed boundaries. There are four USGS streamgages in the Upper Carson that serve as CNRFC hydrologic forecast points (Figure 2). The Upper Carson reached flood stage at all streamgages during 1997,

2005, and 2017 rain-on-snow events. The 1997 event was the record flood event for all three locations as well as at many other locations in northcentral California and western Nevada (Rhoades et al., 2023), with $55 million in projected damages in Douglas County (Thomas and Williams, 1997) alone and over $450 million (unadjusted) in damages across Nevada (USACE, 2013).

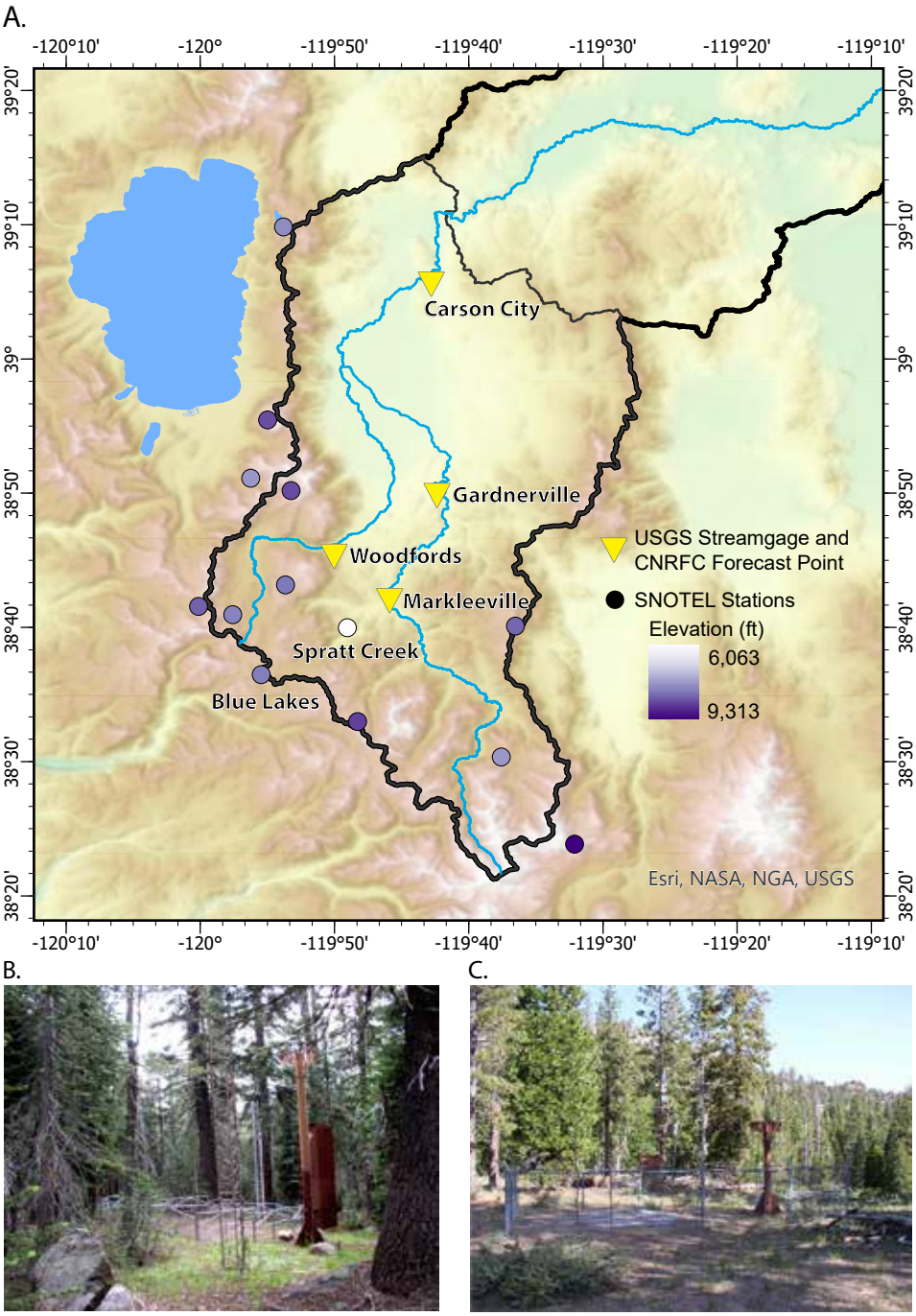

Figure 2: (A) Map of the Upper Carson sub-basin (thin black line) within the Carson watershed (thick black line) with SNOTEL stations (circle) color-coded by elevation and USGS gaging stations and CNRFC forecast points are marked in a yellow upside-down triangle. (B) Photo of the Blue Lakes SNOTEL station. (C) Photo of the Spratt Creek SNOTEL station.

Datasets

NDOT's Drainage Manual outlines design techniques to assess maximum flow through 100-year rainfall and the 100-year flow. Yet this approach does not account for rainfall-derived runoff coupled with snowmelt (NDOT, 2006). Since the Road Weather Information System (RWIS) stations were not designed to assess snow melt, we address this challenge by using data from the SNOTEL stations that monitor hourly precipitation, air temperature, snow water equivalent (SWE), snow depth, soil moisture, and temperature.

SNOTEL data was downloaded and processed using methods outlined in Heggli (2023) for WY2006–2023 at the Central Sierra Snow Laboratory (CSSL) and 9 stations in the Upper Carson watershed: Spratt Creek, Hagans Meadow, Forestdale Creek, Horse Meadow, Burnside Lake, Blue Lakes, Carson Pass, and Ebbetts Pass. Data at three stations (CSSL, Blue Lakes, and Spratt Creek) were hand-cleaned for the period of study and the remaining stations were processed only with automated QC methods Heggli et al. (2022) that were further developed using support from this grant.

Hourly streamflow data was also downloaded from the USGS Water Data Dashboard (`dashboard.waterdata.usgs`) for gaging stations 10311000 (Carson City, NV), 10309000 (Gardnerville, NV), 10308200 (Markleeville, NV), and 10310000 (Woodfords, NV) for WY2006–2023. Monitor and flood stage levels were extracted from the CNRFC graphical river forecast page for each of the forecast points (`https://www.cnrfc.noaa.gov/`).

Assessing ROS across Nevada's Mountains

To assess whether or not hydrologically-impactful ROS events occurred in several locations of Nevada, as well as a first-order estimate of their magnitude, we performed baseflow separation of five streamgages using long-term records of daily data. Baseflow separation is a mathematical deconstruction of the hydrograph into two components, the baseflow and the storm runoff. We define hydrologically-impactful ROS as midwinter responses in storm runoff.

Relevant streamflow data from the headwaters of the Spring Mountains is not available. Therefore, we developed a TWI identification algorithm using the hourly soil moisture for the lowest elevation SNOTEL at Rainbow Canyon (2396 m) at least 50 mm of SWE was present, and manually identified periods of ROS TWI.

Snowpack Runoff Decision Support Thresholds

Identifying Rain-on-Snow Terrestrial Water Input Thresholds

First, we calibrated the previously developed SR-DSS thresholds for terrestrial water input (TWI; the introduction of water to the land surface by rainfall and/or snowmelt) by incorporating data from water year (WY) 2006–2022 at the Central Sierra Snow Laboratory (CSSL) and eight stations in the Upper Carson River watershed (Figure 2). We then apply the SR-DSS to two case studies on data during WY2023. These cases were not included in the learning process using only automated quality control procedures (Level 2; Heggli (2023)) to assess the feasibility and reliability of the SR-DSS in an operational setting. By identifying TWI drivers and antecedent conditions leading to the greatest hydrometeorological impacts at the sub-basin scale (8-digit Hydrologic Unit Code), this approach focuses on furthering the development of a quasi-deterministic SR-DSS.

The methods applied to this paper build off of those developed by Heggli et al. (2022). We continue the focus on ROS TWI, though several modifications were made. After TWI was identified for the period of study, we filtered the data for periods when there was more than 50 mm of SWE during any point in the season, versus the 100 mm threshold before peak SWE. This modification expands the dataset to include ROS events in shallower snowpacks and spring ROS events. The expansion of this framework specifically focuses on antecedent snowpack and present weather for ROS TWI since ROS events are a concern to NDOT.

To identify the patterns of present weather and antecedent snowpack conditions with the potential to produce TWI mid-winter, we analyzed violin plots for snowpack density 1 hr before ROS TWI, 6 hour maximum air temperature, and 6 hour precipitation totals. Following the methods in Heggli et al. (2022), we use the first quartile values as a more conservative threshold for TWI potential. First, the updated thresholds were analyzed for each of the three stations with hand-cleaned data (Figure 3) and aggregated to

identify regional thresholds that integrate the observations at all three stations (Figire 4.a). This analysis intends to review the variation of thresholds across elevations on both windward, the peak, and the lee side of the mountain. Next, we assessed the performance of the thresholds with just the automated QC routines for the remaining stations in the Upper Carson watershed to assess the feasibility of rapidly expanding these methods across all SNOTEL stations in Nevada. Figure 4.b illustrates the identified thresholds for all stations, which agrees with the thresholds identified by the hand-cleaned data.

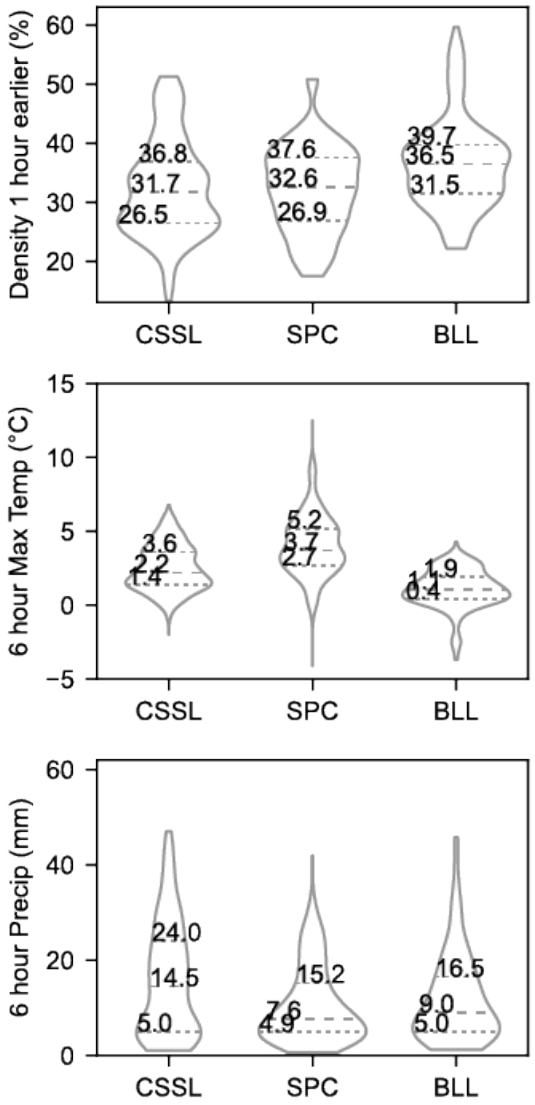

Figure 3: Violin plots of snowpack density 1 hour prior to TWI, 6 hour maximum air temperature, and 6 precipitation totals during ROS TWI for Central Sierra Snow Laboratory (CSSL), Spratt Creek (SPC). and Blue Lakes (BLL).

Updated Thresholds for the SR-DSS

The snowpack density violin plot provides evidence for the formation of preferential flow paths as a uniform wetting front would require the snowpack to evenly absorb all of the rainwater before releasing TWI. At least 75% of ROS TWI at each station occurs before the snowpack is considered "ripe" with a bulk snowpack

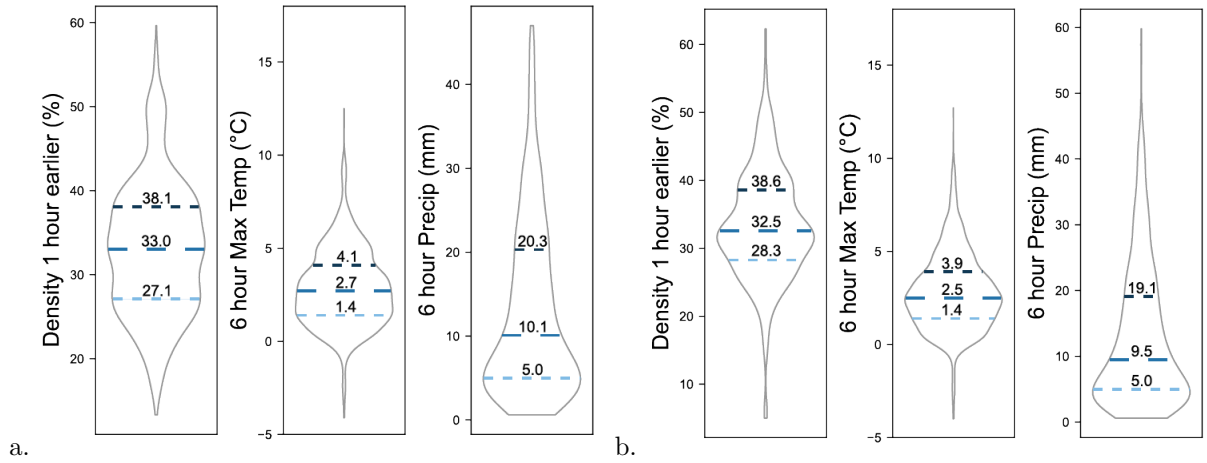

Figure 4: (a) Violin plots of snowpack density 1 hour prior to TWI, 6 hour maximum air temperature, and 6 precipitation totals during ROS TWI for Central Sierra Snow Laboratory (CSSL), Spratt Creek (SPC), and Blue Lakes (BLL). (b) The same as A but for all stations in the Upper Carson study including the CSSL with automated QC routines only.

density greater than 40% (Figure 3.b). The snowpack density thresholds agree between CSSL and Spratt Creek (26.5% and 26.9%) but are substantially higher at Blue Lakes (31.5%). While one might initially think that the higher elevation station has deeper snow, and therefore will need to have a greater snowpack density for the water to make its way through the snowpack, Blue Lakes does not typically have a deeper snowpack than CSSL. The biggest snow years in the period of study (WY2011, WY2017, and WY2019) CSSL had a larger snowpack throughout the entire winter than Blue Lakes. A more plausible explanation of the increased snowpack density could be because precipitation more often falls close to 0 °C at the higher elevation Blue Lakes, and therefore the preferential flow path formation will progress more slowly than in a warmer snowpack, thereby increasing the bulk density of the snowpack (McGurk et al., 1988). While further analysis is needed, this data signals that the snowpack does not need to become fully "ripe" and reach a high density of 40-50 % bulk densities to transmit water from the snowpack to the land surface and thus contribute to flooding. Therefore the lowest station threshold value of 26.5% should be included in the SR-DSS threshold list.

The 6 hour maximum temperature thresholds for ROS TWI potential for each station follow a moist adiabatic lapse rate of 3.7 °C/km with a 2.3 °C difference for the 611 m of elevation difference between Blue Lakes and Spratt Creek (Figure 3.b). Whenever it is raining at Blue Lakes, the rainfall occurring at the lower elevation stations of CSSL and Spratt Creek will always be higher due to the moist adiabatic lapse rate. However, the observations at Blue Lakes show that even when the air temperature is 0.4 °C, there is the potential for ROS TWI. Similar to the snowpack density threshold, this lowest station threshold should be included in the SR-DSS threshold list as it is designed to signal any potential for ROS TWI.

The 6 hour precipitation thresholds for ROS TWI are consistent across all stations at 5.0 mm, 4.9 mm, and 5.0 mm for CSSL, Spratt Creek, and Blue Lakes accordingly (Figure 3.c). The consistency of the values across all stations and the high density of ROS TWI observations at this threshold increase the confidence that 5.0 mm of rain in six hours is sufficient to produce a soil moisture response. The median and third-quartile values also show reasonable agreement between hand-cleaned and automated QC data.

This tool is designed to provide situational awareness, which should include a measure of the likelihood of ROS TWI. The first quartile values have provided insight into a low threshold for ROS TWI. However, crossing the minimum threshold does not necessarily mean that there will be high-impact runoff. To communicate a higher likelihood of ROS TWI we integrate the median and third-quartile values to identify the intersection of the increasing likelihood of ROS TWI response in streamflow. First, we assess the likelihood of ROS TWI based on present weather (Figure 5). The minimum observed air temperature threshold (0.4°C) with the minimum precipitation threshold (5 mm) indicates the lowest potential for TWI on the TWI Potential Scale. Increasing thresholds increase the potential for ROS TWI. The ROS TWI potential

also depends on antecedent snowpack conditions, so we then assess the increase or decrease in TWI potential based on antecedent snowpack conditions. The ROS TWI threshold for density is 28.3%, therefore the ROS TWI potential for the given present weather this snowpack density threshold remains the same. Increasing snowpack density thresholds increase the TWI potential with the warmest and highest intensity rainfall indicating a high potential for ROS TWI regardless of antecedent snowpack conditions. The lowest station snowpack density threshold was 26.5% and higher rainfall totals at higher air temperatures can produce TWI based on the station observations. However, the lower-density snowpack can be slower to respond and therefore the ROS TWI potential decreases for the given present weather potential.

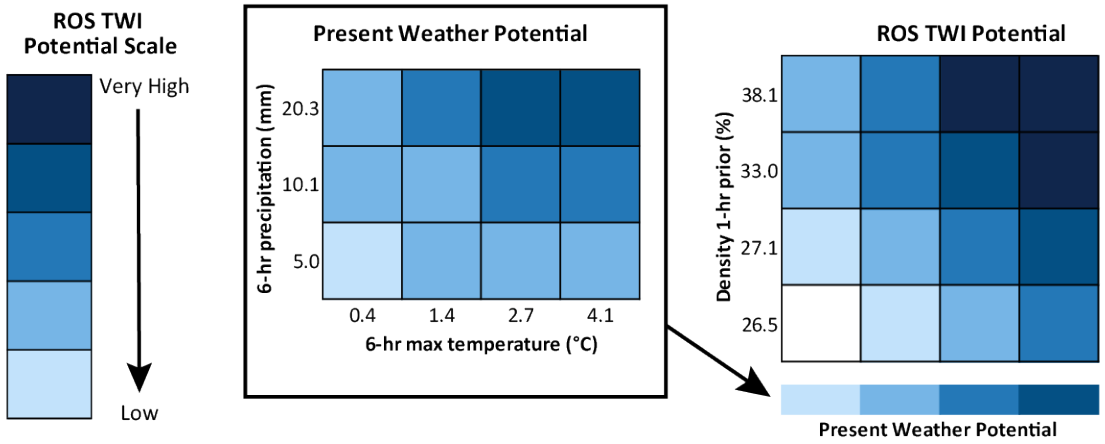

Figure 5: Caption.

Visual Communication

Decision support tools benefit from, if not require, effective visual communication that capitalizes on the efficiency of the visual system to extract information and ensures accessibility to individuals with color vision deficiencies and neurodivergent characteristics (Heggli et al., 2023). For the SR-DSS we integrate color-blind safe color pallets that do not conflict with existing color scales that communicate hazard or impact (Gordon et al., 2022; National Weather Service Western Regional Headquarters, 2022). Following the work of Crameri et al. (2020) regarding the use (and misuse) of colors in science communication, we select a perceptually uniform pallet that varies in lightness to communicate confidence in the potential for TWI (Wilms and Oberfeld, 2017).

Findings and Applications - Nevada Decision Support

ROS Climatology Across Nevada's Mountains

Baseflow separation provides a first-order assessment of ROS climatology and magnitude by identifying the seasons when storm-driven runoff occurs. The baseflow and storm runoff (hereafter runoff) for four different watersheds are shown in Figure 6. The streamflow response in the Carson River (Figure 6.a & c) indicates the presence of perennial baseflow (year-round). There are two peaks in runoff. The largest increases in runoff, which are orders of magnitude larger than baseflows at this time, occur intermittently during mid-winter months with a secondary peak from the spring into summer months. This illustrates (at face value) the Carson River includes all three snowpack runoff types: ROS, midwinter melt, and spring snowmelt. The increases in baseflow during the cool season are transient and follow peaks in runoff; these increases result from ROS or melt events contributing to baseflow after the weather event has occurred.

Baseflow separation at Lamoille Creek in the Ruby Mountains (Figure 6.b & d) shows the dominance of spring snowmelt-derived runoff in driving both runoff and baseflow. Little to no midwinter runoff and with one exception, low midwinter baseflows are observed. While the Carson watershed consistently experiences

ROS and mid-winter runoff, the Ruby Mountains do not yet show evidence of hydrologically-impactful ROS or other mid-winter runoff. This is consistent with the cold, interior, high elevation climate of the northeastern Great Basin. However, as the climate warms and more precipitation falls as rain, it is possible that mid-winter increases in streamflow from ROS and/or midwinter melt will eventually occur here. The lessons learned about ROS hydrology in the highly variable and maritime climate region of the Sierra Nevada can be applied to the spring snowmelt-dominated watersheds as the ROS climatology of Nevada changes.

The small, relatively wet, steep, volcanic, middle-to-high elevation watershed of Third Creek (located on the northeast shore of Lake Tahoe above Incline Village and Highway 431) shows a similar pattern to the Carson River (Figure 6.e & g): occasional peaks in runoff during the cool season before a consistent melt-season signal with a seasonally-dominated baseflow signal during the spring into the summer. In contrast to the Carson River, the magnitudes of baseflow and runoff in Third Creek are much closer in magnitude with typically higher baseflows. This is a product of watershed contributing area, the elevation distribution of the watershed's contributing area, its groundwater hydrology, and water use patterns (little to no pumping compared to the Carson). The largest total flows (baseflow plus runoff) occur during the spring in Third Creek, whereas in the Carson, these flows occur during the midwinter ROS events. But in both cases, midwinter ROS and melt events produce elevated runoff and potentially overland flow impacting infrastructure.

The low-to-middle elevation (between 50 to 8,500 ft) and much warmer and wetter Cosumnes River watershed, located on the western slope of the Sierra Nevada (due east of the Carson River watershed) is shown to provide a comparison with a rain-dominated system (Figure 6.f & h). In the midwinter, ROS is frequent, and much of the watershed can be snow-free. The watershed is sensitive to cold and warm storms with extreme multiday precipitation, but disentangling the roles of hydrometeorology on surface and groundwater behaviors is difficult due to the hydrogeological complexity of the watershed Siirila-Woodburn et al. (2023). In the Cosumnes, runoff occurs throughout the cool season–flow responds to the majority of precipitation events–and baseflow follows a similar cycle throughout the cool season. Baseflows are much more evident in the middle of winter due to the responsiveness of this watershed to precipitation, a stark difference from high-elevation, colder locations such as Lamoille Canyon.

In addition to serving as a comparison location to show a rain-dominated system, the Cosumnes can be interpreted to show the hydrologic characteristics of a much warmer climate in currently snow-dominated with occasional ROS (Carson River and Third Creek) systems. With enough warming–which is possible by end-of-century Rhoades et al. (2023)–even the Ruby Mountains could behave more like the Cosumnes. In all three Nevada watersheds studied, it is recommended to consider the current hazards posed by midwinter runoff but also the potential changes in flood hazard as the climate warms and ROS becomes more frequent. Last, the hydrologic effects of large, moderate-to-high severity wildfire should also be considered. Wildland fire is expected to increasing alter the hydrology and ecologic function of montane watersheds and potentially increase hazards of midwinter runoff via increasing snowpack susceptibility to melt via decreases in snow albedo (more radiation absorbed) and canopy cover (loss of snowpack shading) Hatchett et al. (2023). These effects may elevate baseflows during winter due to more frequent snowmelt as well as increase the potential for ROS-driven melt or preferential routing of rainfall through dense snowpacks.

The assessment of ROS TWI at the lowest elevation SNOTEL station in the Spring Mountains, Rainbow Canyon, identified 13 ROS events that produced TWI when at least 50 mm of SWE was present. Consistent with the findings of (Heggli et al., 2022), the majority of these events did not result in snowmelt. Similarly to the ROS climatology of the Sierra Nevada the ROS events occurred during midwinter months: five in December, four in January, three in February, and one event in early March. The lack of ROS events in March is in part due to the shorter snow-covered season at the station. The snowpack at Rainbow Canyon typically peaks February 28 and is depleted by April 1. Despite the high elevation of the SNOTEL stations in the Spring Mountains, the snowpack is more similar to the lowest elevation SNOTEL in the Sierra Nevada, Spratt Creek, in the Upper Carson where the snowpack typically peaks February 22 and is depleted by March 28. The two other SNOTEL stations in The Spring Mountains, Lee Canyon (2629 m) and Bristlecone Trail (2710 m) also behave more similarly to Spratt Creek than SNOTEL stations at comparable elevations in the Sierra Nevada. The relatively smaller snowpack provides less opportunity for ROS or midwinter runoff, thereby limiting the hydrologic impact of snowmelt-augmented ROS runoff.

To further the assessment of ROS climatology across Nevada, we leveraged the work of Hatchett (2021) to compare seasonal and ephemeral snowpack climatology. Figure 7 highlights the snow-dominated mountain

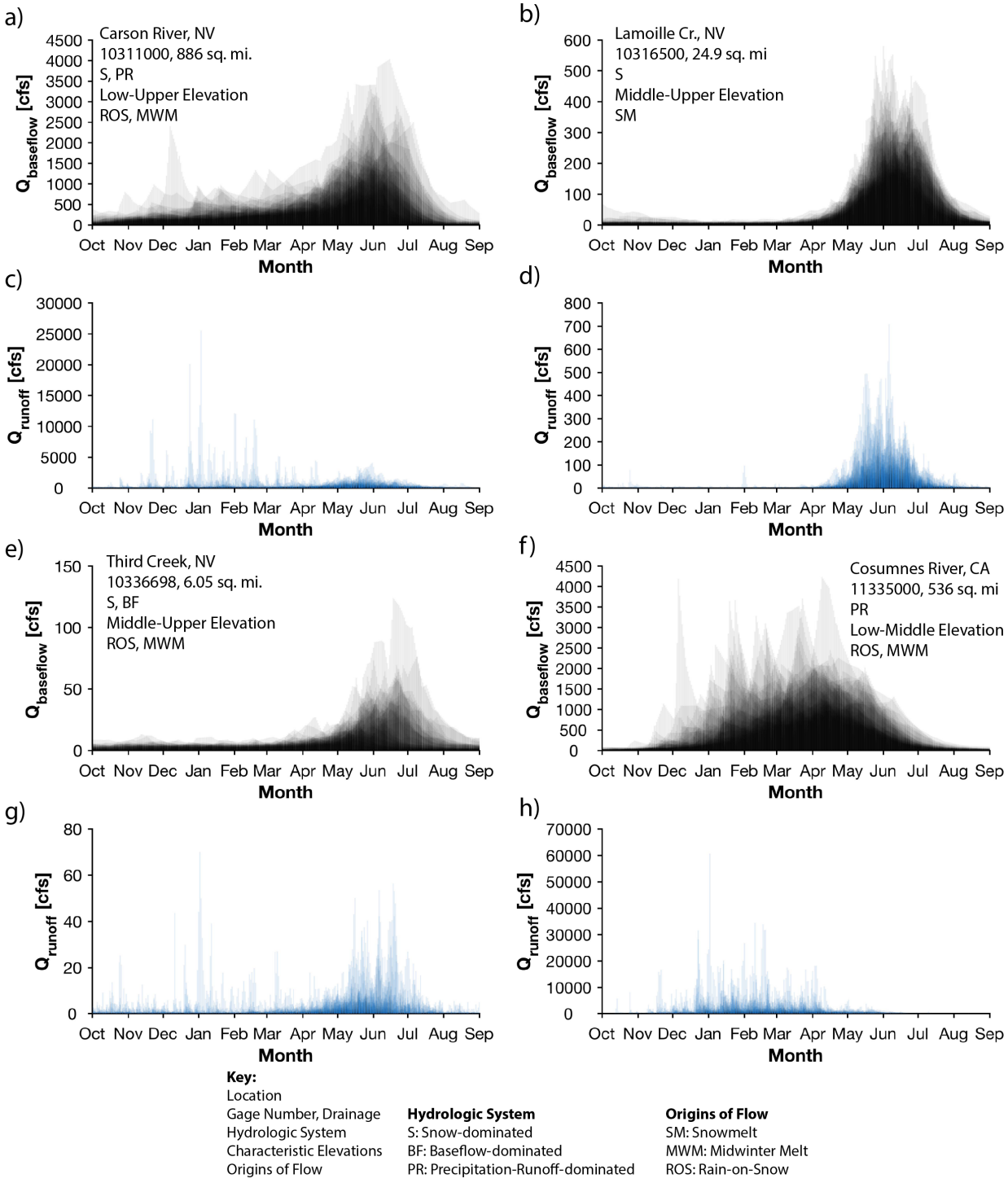

Figure 6: Caption.

ranges across Nevada including the Sierra Nevada, Ruby, and Spring mountains, and emphasizes that these mountain ranges are more ephemeral at lower elevations but the peaks of the mountains have persistent snowpack. The spatial extent of the snow-covered area directly impacts the opportunity for snowmelt-enhanced ROS runoff. The Sierra Nevada and North Eastern Nevada including the Ruby Mountains have a

larger seasonal snow-covered area when compared to the Spring Mountains. Despite evidence of ROS events in the Spring Mountains, there is not as great of a potential for snowmelt-enhanced ROS runoff as there is in the Sierra Nevada Mountains. The Ruby Mountains also have the potential for snowmelt-enhanced ROS runoff, but the atmospheric conditions are not conducive for ROS. However, anticipated changes in precipitation transitioning from snow to rain mean that ROS runoff impacts including localized or even widespread flooding could be expected in coming decades Musselman et al. (2018); Siirila-Woodburn et al. (2021).

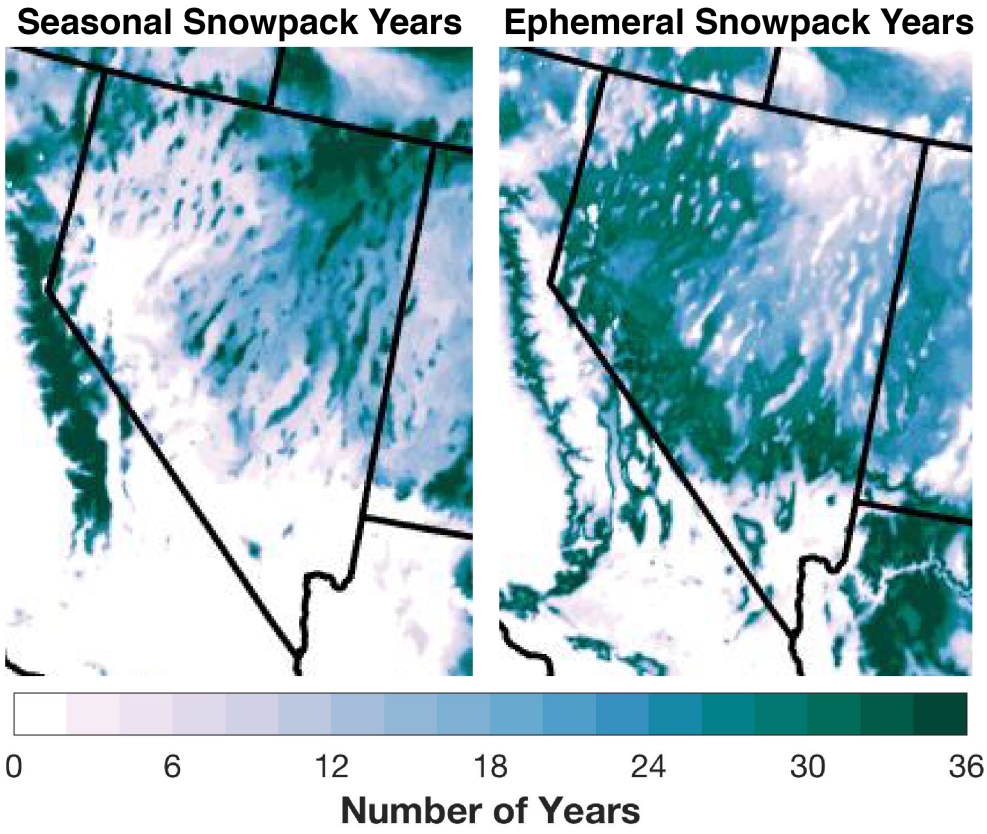

Figure 7: **Seasonal and ephemeral snowpacks are widespread in Nevada.** Left: Seasonal snowpacks are most common in high elevation terrain and eastern Nevada. Right: Ephemeral snowpacks occur most frequently in the lower elevations of western and southern Nevada. Snow seasonality maps are based on 36 years of gridded snowpack data (Hatchett et al., 2021).

SR-DSS

Test Case Assessment of SR-DSS

The objective of SR-DSS is to run operationally in real-time. To assess the reliability of the tool in an operational environment, we apply only the automated QC methods (Level 2; Heggli (2023)) and assess data from WY2023 that was not included in the development of the SR-DSS thresholds. In addition to the test case assessments, we applied the SR-DSS to seven events from WY2006–2022 in Appendix A. Four events reached flood stage at any of the four CNRFC forecast points: 29 December 2005–1 January 2006; 7–10 January 2017; 6–11 February 2017; and 6–9 April 2018. We included three ROS events that did not cause flooding: 13–15 February 2019; 9–12 December 2022, and 26–28 December 2022. We focus on one ROS test case in WY2023: 29 December 2022–1 January 2023. To aid in the regional assessment of the SR-DSS, we developed a regional map that includes all of the SNOTEL stations in the Central Sierra Nevada and color code the TWI potential at each station using the updated SR-DSS thresholds with the Level 2 data. Blue

Lakes and Spratt Creek are noted on the map and active TWI is indicated with a thick black outline of the SNOTEL station. The regional map also includes the four CNRFC forecast points that are color-coded for monitor and flood stage. Each event will be discussed in detail in the following sections with figures that include three regional maps of TWI potential and streamflow response in the top panel (1A, B, and C) for selected times indicated with a pink vertical line in the lower panel (2A and B). The lower panel (2) shows the time series data from the Blue Lakes (2A) and Spratt Creek (2B) leading up to the streamflow response. The time series plots include 1 hour and 6 hour precipitation totals and 1 hour and 6 hour maximum air temperature in the top panel. The second panel shows bulk snowpack density and SWE overlayed with the SR-DSS TWI potential is below that. The next panel shows soil moisture at 5 cm, 20 cm, and 50 cm depths with periods of active TWI highlighted in pink, and finally the maximum hourly stream flow at the four CNRFC forecast points in the Upper Carson River. This figure is provided for each test case and the events included in Appendix B.

29 December 2022–1 January 2023

From December 2022 and January 2023, the Sierra Nevada experienced nine back-to-back storms that predominately produced snowfall at the SNOTEL station elevations. Two of these events (29 December 2022 and 10 January 2023) were ROS events, but only the 29 December 2022 event resulted in flooding on the Carson River and will be the focus of the first test case (Figure A.7). The snowpack at Blue Lakes (396 mm of SWE) and Spratt Creek (122 mm of SWE) was well above normal for the time of year. Ahead of this event, the depth-averaged soil moisture at Blue Lakes was below the period of record median and was about average at Spratt Creek. Prior to the ROS event, the region experienced anomalously high temperatures 24–26 December 2025 with maximum air temperatures at Blue Lakes ranging from 8.2–10.1 °C. A system moved into the region around midnight on December 26th that brought snowfall to Blue Lakes keeping the snowpack density relatively low at 29% and rain to Spratt Creek that increased the density to 33% (Figure A.7.2A and B).

The air temperature at Blue Lakes was below freezing when the precipitation first started on 29 December 2023 but by 11:00 PST the following day the temperature threshold was met for Low ROS potential and at 17:00 PST the air temperature was 0.5 °C for the second consecutive hour and TWI had initiated at 20 cm and 50 cm depths (Figure A.7.1B). The ROS TWI air temperature threshold was not met for another three hours. This is evidence that the air temperature threshold should be adjusted for elevation and the 0.4 °C 6 hour maximum threshold for Blue Lakes may be more effective at predicting ROS TWI (Figure **??**). As the air temperature increased to meet the ROS TWI potential threshold, Blue Lakes continued to produce TWI until ROS TWI potential thresholds were no longer met and downgraded to low ROS TWI potential. At 10:00 PST on 31 December 2023 the air temperature at Blue Lakes had dropped to 0 °C and TWI potential transitioned from low ROS to none after multiple hours of the air temperature being below the ROS TWI threshold (Figure A.7.1C). TWI occurred for a total of 12 continuous hours at Blue Lakes though there is no evidence of snowmelt since SWE continuously increased throughout the storm.

On 30 December 2023 at 05:00 PST the ROS TWI thresholds were met at Spratt Creek and TWI initiated two hours later as SWE began to decline (Figure A.7.1A). SWE continued to decline as soil moisture continued to register TWI until 10:00 on 31 December 2023 when air temperature dropped to 0.2 °C and SWE began to increase as density started to decrease indicating precipitation had transitioned from rain to snow. However, the 6 hour maximum air temperature threshold was still above 1.3 °C for another two hours before downgrading to Low ROS and then to no potential. TWI was active for a total of 20 hours at Spratt Creek and there is strong evidence of snow melt since the already dense snowpack lost SWE as soon as rain started. There is evidence that the rain was warm enough to melt the snowpack since the air temperature during precipitation on 30 December 2023 ranged from 3.6-6.8 °C.

Lower in the watershed, streamflow on the East Carson at Markleeville and Gardnerville began to slowly increase at the same time precipitation started at Spratt Creek. By the afternoon on 31 December 2022 the Garnerville station reached monitor stage and continued to steadily rise until hitting flood stage 5 hours later. The peak coincided with the drop in air temperature and the transition from rain to snow at both Blue Lakes and Spratt Creek around 10:00 on 31 December 2022 (Figure A.7.1C). Despite Gardnerville reaching flood stage, Markleeville and Carson City were just shy of monitor stage.

SR-DSS Assessment

To assess the reliability of the SR-DSS for real-time communication, this case study demonstrates that the automated Level 2 data can perform sufficiently for this event. However, neither event caused a snow plug in the precipitation gauge. 2023 January 4th the Blue Lakes precipitation gauge did plug and inhibited the gauge to record new precipitation for 16 days. One advantage of using the Level 2 data for ROS events is that most major sensor issues occur during snowfall. Snow depth sensors struggle to measure during heavy snowfall (Anderson and Wirt, 2008), snow plugs only occur with snow or mixed-phase precipitation that sticks and accumulates to the side of the precipitation gauge, and bridging of the snow pillow will not register new snowfall. If a snow plug has not released before a ROS event, sufficient rain can release the snow plug and regain accurate and timely precipitation observations (Heggli et al., 2022). Complex structures like melt-freeze crusts that cause bridging over a snow pillow can also be released by rainfall (Heggli et al., 2023). Because the Level 2 QC process integrates automated flagging of suspect data, the formation of snow plugs and bridges could be tracked to notify potential data users that the data may not be reliable.

To test the reliability of automated quality control processed data to establish SR-DSS thresholds, we performed the pattern recognition on those data for CSSL, Blue Lakes, and Spratt Creek (Figure 9). The automated processed (Level 2) derived SR-DSS thresholds only have slight changes from the Level 3 hand-cleaned derived thresholds. Although more stations should be developed manually to confirm the reliability of the Level 2 data for automated threshold analysis, this first assessment demonstrates the utility of the Level 2 data in providing situational awareness for mid-winter snowpack runoff.

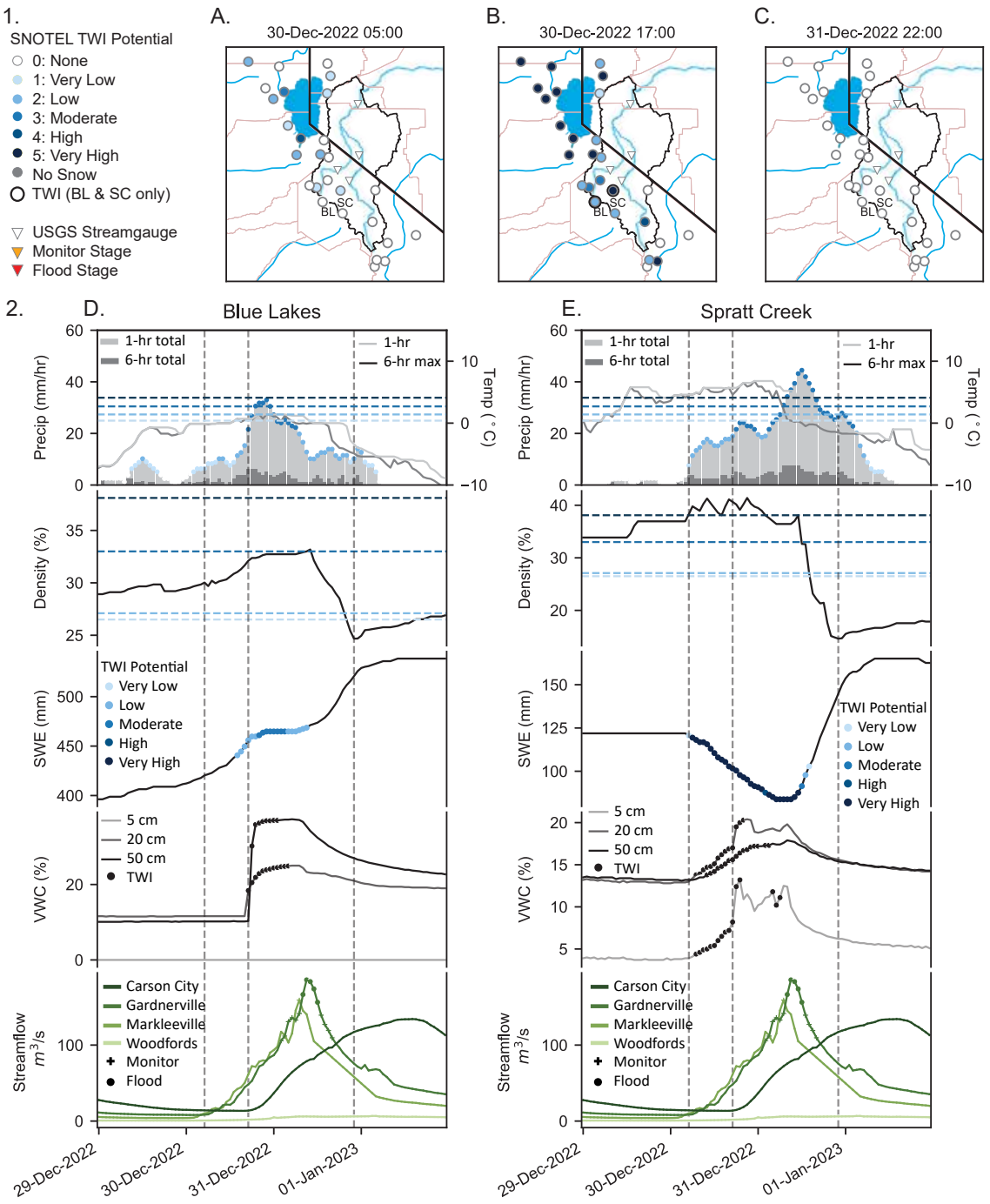

Figure 8: 29 December 2022–1 January 2023: Regional maps of TWI potential and streamflow response (1A, B, and C) for selected times indicated with a pink vertical line (2A and B). Time series data from the Blue Lakes (2A) and Spratt Creek (2B) leading up to the streamflow response. There are four panels: 1 hour (dark grey) and 6 hour (light grey) precipitation totals and 1 hour (dark grey) and 6 hour (light grey) maximum air temperature in the top panel; shows bulk snowpack density color coded to communicate increases (pink), decreases (grey), and no change (white) in density values each hour; SWE (black) overlayed with the SR-DSS TWI potential (low ROS in light blue, ROS in dark blue, low W/SDM in light orange, and W/SDM in orange); soil moisture ranging from light to dark grey at 5 cm, 20 cm, and 50 cm depths accordingly with periods of active TWI highlighted in pink; maximum hourly stream flow in green ranging from dark to light green in the following order: Carson City, Gardnerville, Markleeville, and Woodfords.

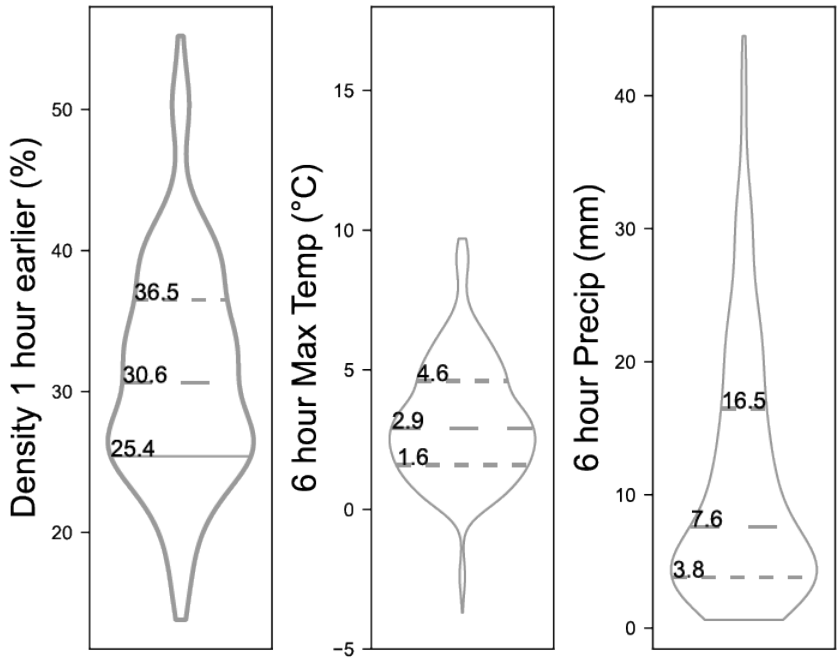

Figure 9: Violin plots of snowpack density 1 and 6 hours prior to TWI, 6 and 12 hour maximum air temperature, and 6 and 12 hour precipitation totals during ROS TWI (blue) and W/SDM TWI (orange) for Blue Lakes (BL), Central Sierra Snow Laboratory (CSSL), and Spratt Creek (SC) using Level 2 automated QA/QC process from Chapter 3.

Research Approach - Western State Explorations

This section describes the creation of a new dataset relating observed surges in streamflow to the weather conditions that preceded the surge. We then classify those weather conditions as ROS-induced or non-ROS induced based on variable thresholds described later in this section. To create this dataset, we aggregate streamflow measurements and weather data through regional associations. The dataset is then used to compare surge size in ROS and non-ROS induced floods. Table 1 describes the data sources used to obtain the relevant variables.

Table 1: Data sources used in the creation of the stream surge dataset.

Source	Abbr.	Description	Reference
United States Geological Survey	USGS	Streamflow data for 2,586 streamgages at a sub-hourly level and gage flood stages, when available.	USGS (2023)
Snowpack Telemetry Stations	SNOTEL	Daily weather data from 808 stations, used to identify conditions for ROS events.	NOAA (2016)
Watershed Boundary Dataset	WBD	Hydrologic unit code (HUC) shapefiles at the HUC 8 level.	USGS (2024a)
Parameter-elevation Regressions on Independent Slopes Model	PRISM	Modeled weather data for comparison with and verification of SNOTEL measurements.	NACSE (2024)

Streamflow, SNOTEL, and PRISM data are accessed through functionality available in the `rsnodas` package (Schneider, 2023). Data collection is limited to the area encompassed by the 11 Western states shown in Figure 10.

Streamflow Peak Detection

Our primary interest in the streamflow measurements is identifying peaks, or surges, in the streamflow. These peaks are identified using a peak detection algorithm available in the the `cardidates` (Rolinski et al., 2007). We feed hourly maximum measurements of streamflow into the algorithm, and use linear interpolation to impute any missing values in the time series for each streamgage. We note that missing streamflow measurements are sometimes the results of flow rising to unusually high levels, causing gage sensors to malfunction (USGS, 2018, 2024b). Future research should consider alternative missing value imputation approaches to account for potentially missed stream surges due to gage malfunction.

The peak detection algorithm requires the user to provide a user-defined flow threshold for each gage. Whenever they are available, we use predefined flood stages for this threshold. The National Weather Service defines flood stage as "the stage at which overflow of the natural banks of a stream begins to cause damage in the local area from inundation (flooding)" (USGS, 2023). Predetermined flood stages are published online by the USGS for 737 of the 2,586 streamgages originally involved in our study (28.5%). Flood stages for the remaining 1,849 gages are estimated by identifying the streamflow measurement marking the 75th percentile of the annual maximum reported measurements for each unique location. The selection of the 75th percentile is somewhat arbitrary, and is meant to target an extreme surge event for which there is a reasonable number of observations exceeding the threshold. Future work should consider alternative methods for imputing flood stage thresholds when that information is not available.

After defining existing/estimated flood stages for each streamgage, we implement the peak detection algorithm and identify peaks at 2,199 of the 2,348 available streamgages using each streamgage's full period of record (i.e., the time span over which data is recorded). We detect a total of 60,811 peaks between all the streamgages. Of these 60,811 peaks, 55,207 are reported at streamgages with estimated floodstages (90.8%).

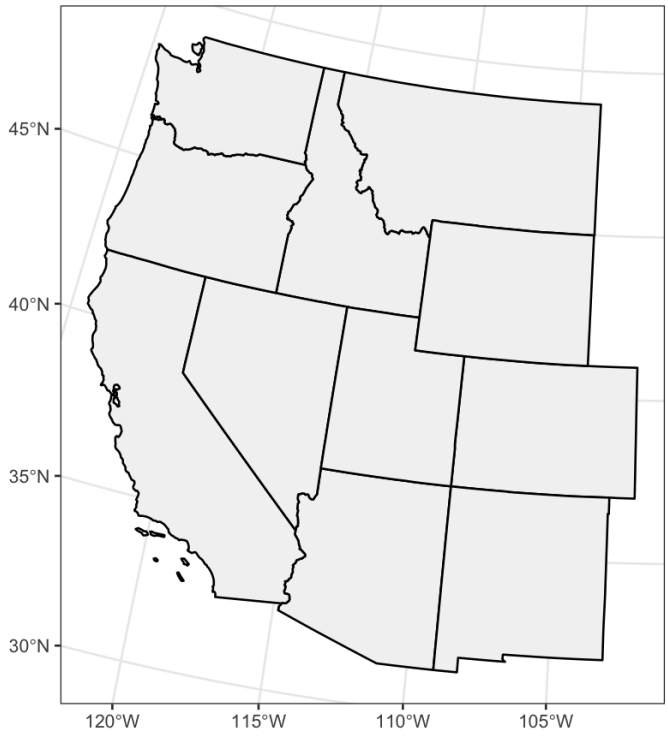

Figure 10: Map of the states in our region of interest, including Washington, Oregon, California, Nevada, Idaho, Utah, Arizona, Montana, Wyoming, Colorado, and New Mexico.

Baseflow Calculation

In order to examine differences in streamflow surges between ROS and non-ROS peaks, we obtain a baseflow (b_f) measurement preceding each peakflow (p_f) measurement and define stream surge (g) as

$$g = \frac{p_f}{b_f}. \tag{1}$$

Peakflow measurements for each streamgage are reported by the peak detection algorithm along with the timestamp. We calculate baseflow by finding the median of hourly streamflow measurements at the relevant streamgage in the two week period prior to the flood peak. For instances where two peaks occur in a time period shorter than two weeks, we adjust the algorithm to use the median of the streamflow measurements in the time between the two neighboring peaks to describe the baseflow of the latter peak.

Weather Data

Weather data measurements are obtained at a daily level for 808 SNOTEL stations across the 11 states of interest. The specific variables we use to inform ROS flood classification and surge representation include the following:

- temperature (temp in °C)
- precipitation (precip in mm)
- snow depth (SD in cm)
- SWE (SWE in mm)
- soil moisture (SM as percentage)

- elevation (m)
- snow melt (melt in mm)

SNOTEL stations use devices called snow pillows to measure SWE, which describes the water content available in the snowpack (USDA, 2024). Snow melt (s_m) is not a variable reported directly by SNOTEL stations, so we calculate it using measured precipitation and SWE. This calculation is performed as follows:

$$s_m = (p + s_{w_d}) - s_{w_{d-1}}, \tag{2}$$

where s_w represents SWE, p represents precipitation, and d represents day. s_{w_t}. This calculation assumes that measured precipitation is equivalent to the increase in the water content of the snowpack on days with no snow melt. Any bias in measurements of precipitation or SWE would thus be reflected in this calculation. Future research should compare this calculation to modeled estimates of snow melt such as those available in SNODAS (NSIDC, 2024). This snow melt measurement is used in the Musselman et al. (2018) ROS classification framework described later.

Data Associations

The USGS's HUC system divides the United States into a set of drainage basins at six different spatial scales, ranging from continental (HUC 2) to local (HUC 12). A drainage basin, or watershed, is an area of land that captures precipitation and channels it into a creek, river, or stream, eventually leading to the ocean (Seaber et al., 1987). In order to associate the streamgages and SNOTEL stations in our dataset, we group them together by HUC 8 watershed boundaries. We only retain measurements contained in watersheds that have at least one SNOTEL station and at least one streamgage. Connecting streamgages and SNOTEL stations in this way assumes that measured water at SNOTEL stations will flow to the streamgages located in the same HUC 8 basin. After associating streamgages and SNOTEL stations by HUC region, only 7,807 of the 60,811 (13%) peaks remain for analysis at 1,279 unique streamgages. Of these remaining peaks, 4,977 (64%) are reported by streamgages with estimated flood stages. This considerable post-association decrease as well as intermediary decreases in usable SNOTEL station and streamgage counts are shown by Table 2 and illustrated spatially in Figure 11.

Table 2: SNOTEL station and streamgage counts at each step in the data refinement process.

Processing Step	**SNOTEL Count**	**Streamgage Count**
Initial	808	2,586
Post-Download	808	2,384
Post-Peak Detection	808	2,199
Post-Association	726	1,279

We see from both Table 2 and Figure 11 that we retain just over half of the available streamgages post-association. Future work will consider alternative approaches, including the use of gridded climate products such as SNODAS (NSIDC, 2024), to expand the analysis to include streamgages beyond those considered in this study. Despite the data loss, exploration at the HUC 8 spatial scale allows us to target streamgages in mostly mountainous areas prior to flood control measures (i.e., dams), which are likely the streamgages most sensitive to fluctuations from ROS events.

Daily ROS Event Classification

Musselman et al. (2018) defines a ROS classification scheme that focuses on ROS events with the potential to produce flooding. We implement this method using historical precipitation values reported by SNOTEL stations. This method requires that the following three conditions be met in order to positively classify a ROS event:

1. $s_w \geq 10mm$
2. $p \geq 10mm$

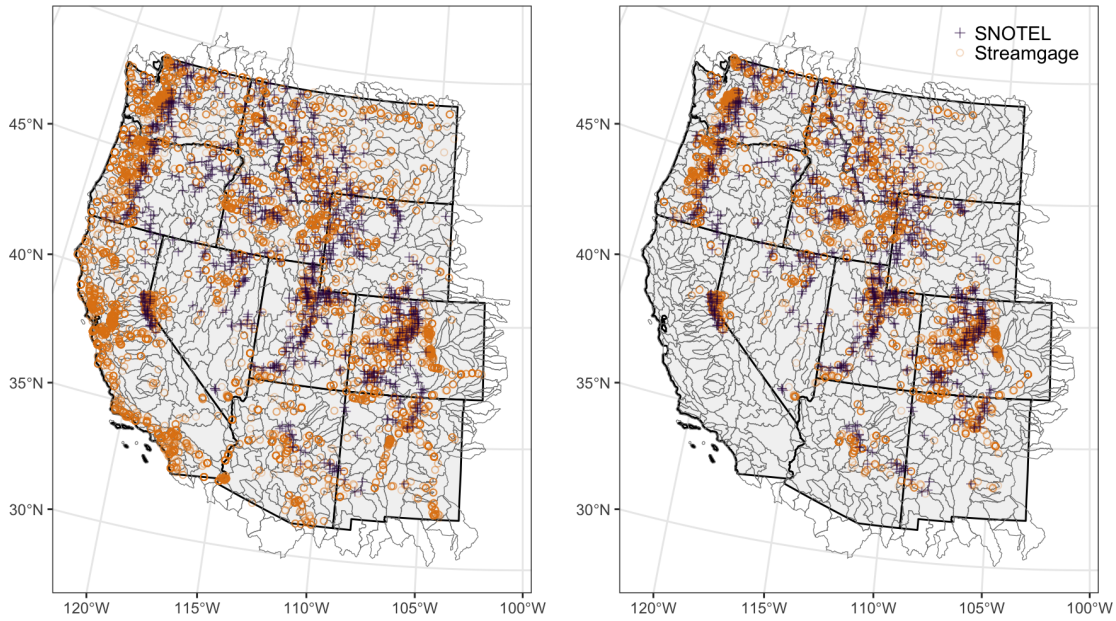

Figure 11: Streamgage locations and SNOTEL stations before (left) and after (right) being associated by HUC region. Those remaining after association are the only ones considered in the final analysis. Numeric decreases describing this visual are given in the last two rows of Table 2.

3. $s_m/(p + s_m) \geq 0.2$

where p is precipitation, s_w is SWE, and s_m is snowmelt. After identifying days when ROS event conditions have been met at individual SNOTEL stations, we determine whether a day qualifies as a ROS event at the HUC 8 level by requiring that at least half of the SNOTEL stations within the HUC region fulfill the requirements for a ROS event to occur. We then classify peaks as ROS-induced if they occur within seven days of a ROS event day in their respective HUC region. Of our remaining peaks, 2,725 are classified as ROS-induced (34.9%) and the remaining 5,082 (65.1%) as non-ROS induced. Figure 12 shows the distributions of surge magnitude in ROS and non-ROS induced floods classified using this method. We see that non-ROS induced surges tend to be considerably smaller than those that are ROS-induced, and that the overall surge distribution most closely resembles the distribution of non-ROS induced surges.

We also explore the different distributions of the weather conditions preceding a stream surge for both ROS and non-ROS events in Figure 12. The distributions of temperature, precipitation, and SWE are shown to highlight differences between ROS and non-ROS behaviors. We see that temperatures for ROS-induced peaks tend to be around 2.8 degrees lower than those that are non-ROS induced, possibly due to the time periods throughout the year in which both peak types are more likely to occur. The left skew in ROS compared to the right skew of the non-ROS precipitation measurements indicates that for surges classified as ROS-induced, precipitation measurements tend to be substantially larger. ROS and non-ROS follow similar distributions for SWE.

However, Figure 12 ignores the spatial structure inherent in the data, as ROS events do not occur at the same rate across the Western states. Figure 13 visualizes the spatial distribution of surge counts and relative surges attributed to ROS events in the region of interest. We see that there is a higher proportion of ROS surges in the Northwest, suggesting that ROS events tend to occur more frequently in mountainous regions near the coastline. It also shows that the overall surge count per year by HUC region doesn't follow a clearly identifiable pattern across the region of interest.

We investigate the months in which ROS and non-ROS induced surges are most likely to occur in Figure 14. We see that the majority of non-ROS induced flooding occurs during spring and summer months, specifically in May and June, likely in the form of spring runoff. In contrast, ROS-induced floods seem to occur in roughly equal proportions from November to January as well as May.

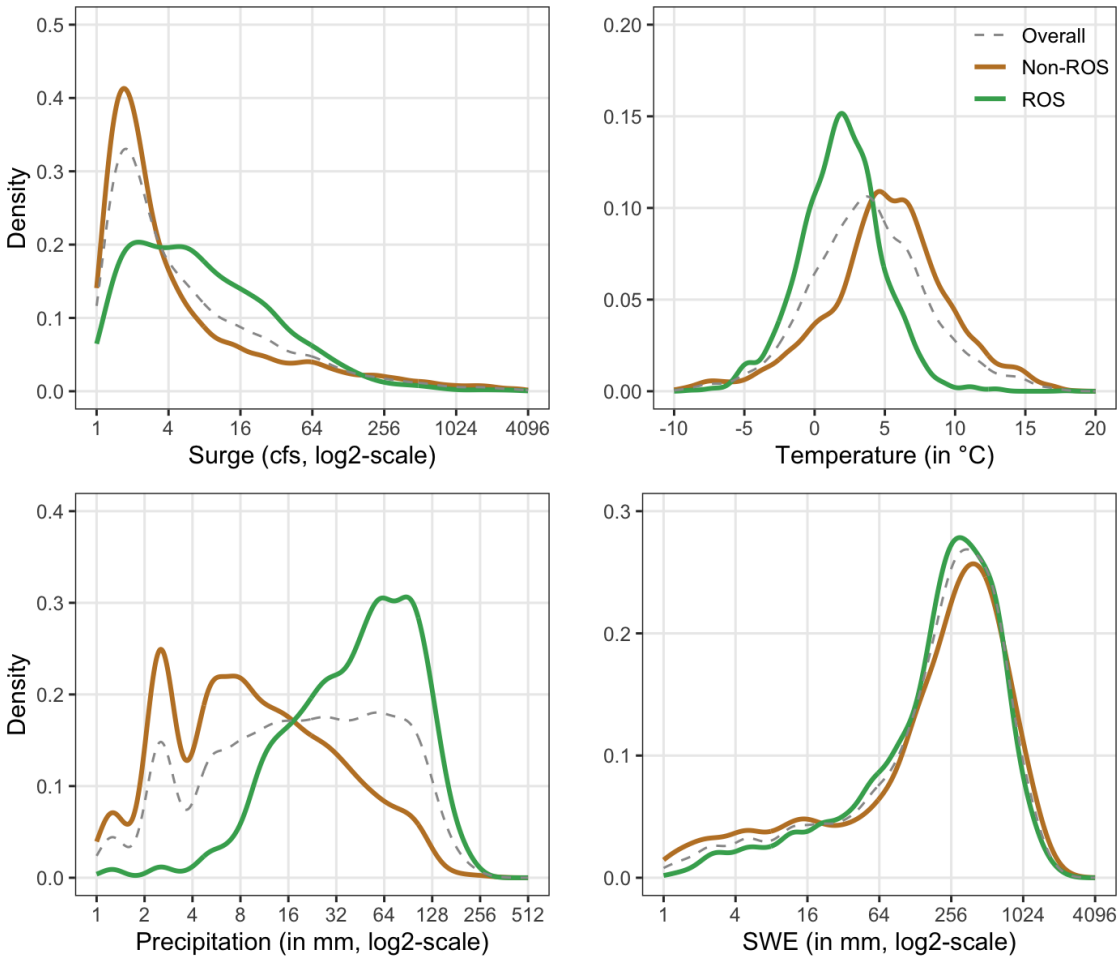

Figure 12: Densities of ROS vs non-ROS classified streamflow surge, temperature, precipitation, and SWE measurements in comparison with the overall distribution of these variables.

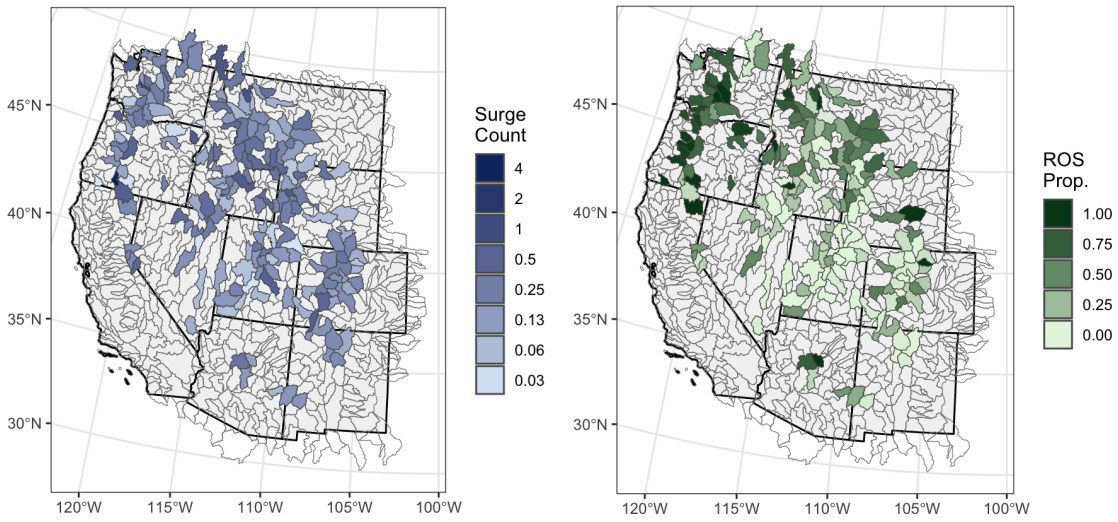

Figure 13: Choropleth maps comparing overall surge count per year in each HUC region (left) to the proportion of the surge count that is ROS-induced (right). Surge count per year is found by counting the total number of surges at a given streamgage and dividing it by the number of years in its period of record. If there are multiple streamgages in a given HUC region, the median surge count per year is retained.

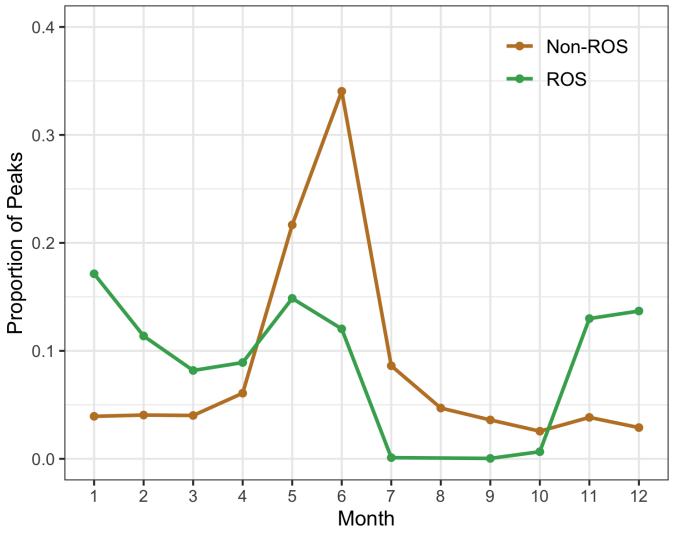

Figure 14: Proportions of total peaks occurring in each month by ROS classification.

We next examine the distribution of the ratios of ROS vs non-ROS induced surges. This ratio is calculated for an individual streamgage as follows:

$$r_r = \frac{g_r^{(m)}}{g_n^{(m)}}, \tag{3}$$

where r_r is the "ratio of ratios", $g_r^{(m)}$ is the median (i.e. middle value) of all ROS-induced surges, and $g_n^{(m)}$ is the median of all non-ROS induced surges. Only the 245 streamgages with at least two non-ROS and ROS peaks are considered in the final distribution, shown in Figure 15. Due to our relatively small sample size of peaks and the inherently sensitive nature of ratio calculations, $\bar{r}_r$ tends to be overly influenced by outlier observations. In the following section, we model these ratios and their resulting distribution in an effort to smooth out inconsistencies between locations and provide a more stable quantification of the relationship between ROS and non-ROS induced surges.

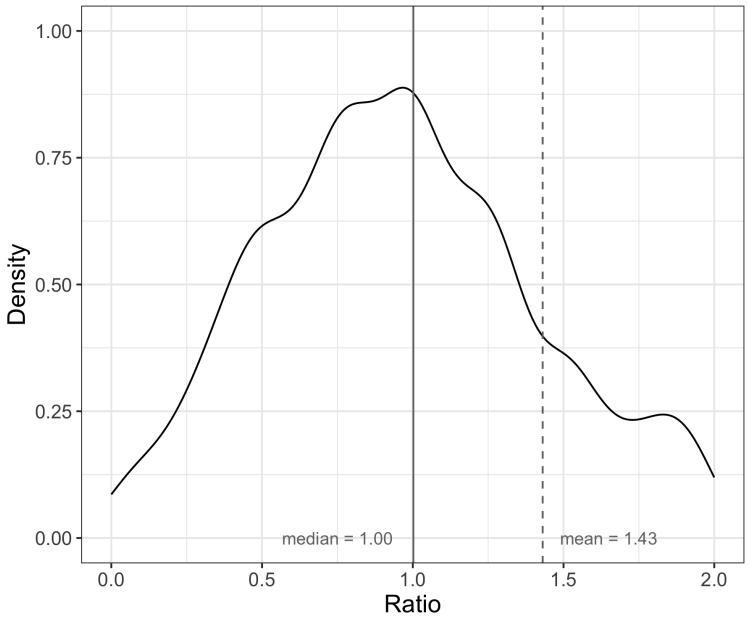

Figure 15: Distribution of empirical ratios of ROS induced surge to non-ROS induced surge measurements at streamgages with qualifying peaks, with the x-axis truncated at 2 to exclude outlier measurements.

Figure 16 shows the full range of these empirical ratios, with the largest outlier indicating that there was one streamgage whose ROS surges were 30 times as large as its non-ROS surges.

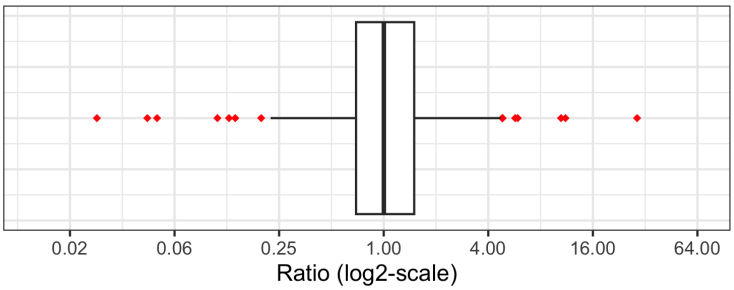

Figure 16: Boxplot illustrating the full range (on a log scale) of the distribution of empirical ratios from Figure 15.

We also consider the ratio of peakflow measurements between ROS and non-ROS induced floods, shown

in Figure 17. As indicated by the medians of both distributions in Figure 15 (1.01 and 1.00 respectively), there does not seem to be a notable difference in extremes between ROS and non-ROS induced surges. We investigate this difference further in the following section.

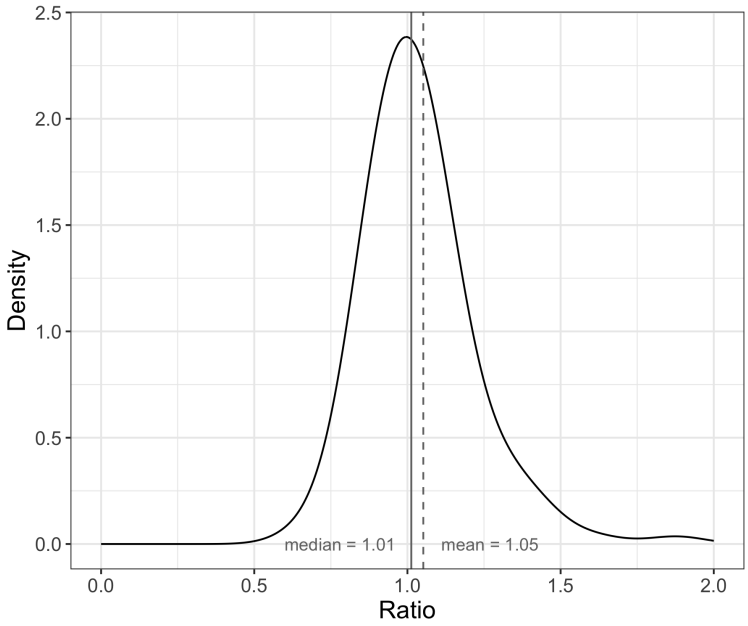

Figure 17: Distribution of empirical peakflow ratios of ROS induced surge to non-ROS induced surge measurements at streamgages with qualifying peaks.

Database Description

For each of the 7,807 remaining flood peaks in our analysis, we link weather variables to the streamgage of a peak's occurrence by calculating summaries of measurements from SNOTEL stations located in the same HUC region for the five days prior to the datetime reported by the peak. We assume the dependence of streamflow response upon the accumulation of precipitation, snow depth, etc. during the five days leading up to the peak. For each weather variable, values for all SNOTEL stations within the relevant HUC region over the given time period are collected and the median of the following summary statistics is calculated separately for each station: mean, median, minimum, and maximum. The sum of precipitation over this time period is also calculated. The overall median value for the entire HUC region for each summary statistic is then added to the data frame containing peak information. We include an example of this aggregation for a single ROS-induced streamflow peak near Reno, Nevada on February 10, 2017. The map in Figure 18 shows the spatial distribution of the SNOTEL stations and streamgage within their HUC 8 boundary.

We describe the aggregation of data required to connect SNOTEL weather data with the streamgage in Table 3. This example only shows the aggregation for the means of each weather variable to demonstrate the workflow—median, minimum, and maximum measurements are also computed in a similar manner and stored within the database.

The 'HUC' column in Table 3 represents the specific values appended to this peak observation in the peak data frame. This aggregation is performed for each of the 7,807 peaks. Additional relevant variables in the final data frame used for analysis include peakflow, baseflow, surge, ROS classification, randomly assigned cross-validation (CV) group, and the geographic location (i.e., longitude and latitude) of the streamgage at which peak occurrence is observed. Overall, there are 49 variables associated with each peak observation. A list of all variables and the summaries applied to the weather variables is available in Table 4.

The final dataset connects weather measurements to streamflow surges through HUC association to establish spatial dependencies, allowing us to meaningfully investigate streamflow response to weather behavior. It also contains information about ROS classification for each peak, which provides us with not only

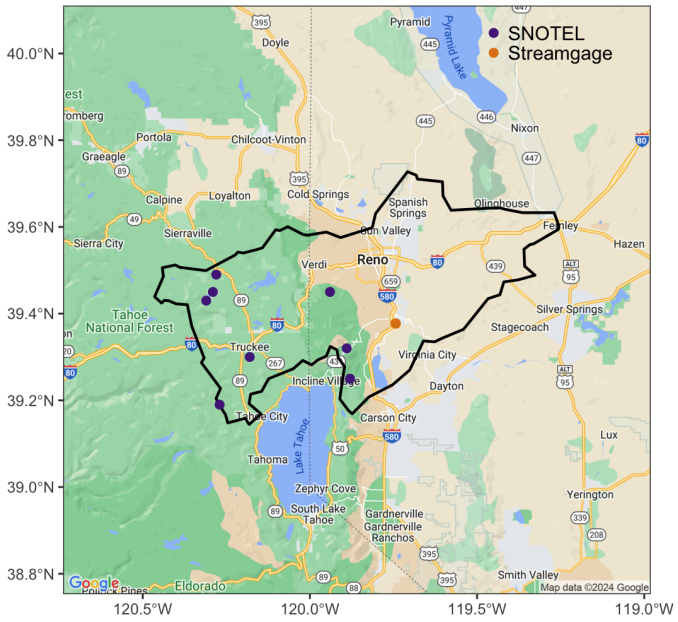

Figure 18: Map of HUC 16050102 with its SNOTEL stations (IDs: 340, 1242, 652, 539, 540, 541, 784, 809) and the streamgage (ID: 10349300).

Table 3: Example of data aggregation by HUC region for a singular peak. Mean measurements are found at each station (for the 5 days prior to peak occurrence). The 'HUC' column contains the watershed-level medians of the station-level mean measurements for each variable, which include Temperature (Temp), Precipitation (Precip), Snow Water Equivalent (SWE), Snow Depth (SD), Soil Moisture (SM), Snow Melt (Melt), and Elevation.

	SNOTEL Station Mean Measurements by ID								
Variable	**340**	**1242**	**652**	**539**	**540**	**541**	**784**	**809**	**HUC**
Temp ($°C$)	0.4	4.4	-0.8	2.1	2.7	-0.3	0.5	2.8	**1.3**
Precip (mm)	22.4	40.1	55.4	33.5	31.5	40.6	57.4	37.6	**38.9**
SD (mm)	2520	1176	4328	1492	1128	3846	2886	1514	**201.7**
SWE (mm)	845	439	1408	448	374	1273	1386	470	**658**
SM (8-in %)	25.0	39.6	8.3	21.2	30.7	19.4	39.7	36.7	**27.8**
SM (20-in %)	17.7	39.3	9.5	25.0	28.2	19.6	27.4	38.7	**26.2**
Melt (mm)	0	39.1	7.6	26.9	29.4	0	1.0	36.1	**17.3**
Elevation (m)	2510	1979	2683	2128	1962	2541	2442	2072	**2285**

Table 4: List of variables and their associated statistical summaries included in final dataset.

Variable	Minimum	Maximum	Median	Mean	Sum
State					
ID					
HUC					
Datetime					
Peakflow					
Baseflow					
ROS Class					
Surge					
Temp	X	X	X	X	
Precip	X	X	X	X	X
SD	X	X	X	X	
SWE	X	X	X	X	
8-inch SM %	X	X	X	X	
20-inch SM %	X	X	X	X	
Melt	X	X	X	X	
Elevation	X	X	X	X	
CV Group					
Coordinates					

a better understanding of the characteristics of ROS-induced floods, but also a better understanding of the relationship between ROS and non-ROS floods and what distinguishes their behavior. The following section demonstrates an application of this dataset to model the ratio of ROS to non-ROS induced surges, in order to better quantify the differences between ROS and non ROS-induced stream surges.

Findings and Applications - Western State Explorations

In this section, we use the finalized database to quantify the relative difference in stream surges associated with ROS and non-ROS events. Recall in Figure 15 the highly skewed distribution of the empirical ratios between ROS and non-ROS induced surges at individual streamgages. We create a generalized additive model (GAM) for representing stream surge with the intent to provide a more accurate and stable indicator of stream surge differences while controlling for location-specific dependencies.

Model Selection

GAMs are an adaptation of a linear model that permits nonlinearity in the prediction of the response variable through the use of data-driven smoothing functions (Hastie et al., 2009). In our case, GAMs are able to characterize the non-linear relationships that weather and location share with stream surge. Due to the highly skewed distribution of surge measurements, likely resulting from the drastically differing stream sizes included in our analysis, we elect to use the log of surge as our response variable and convert back to original units after generating modeled results.

As an initial step in the modeling process, we determine which of the 38 eligible explanatory variables from the peak dataset are the most important in predicting the log of surge through a combination of tests for statistical significance and practical viability. For example, we remove soil moisture percentage measurements from consideration for practical purposes, since over 80% of peak observations report it as missing. This is unfortunate, since soil saturation is a direct contributor to increased runoff from ROS events and promises high levels of significance within our model, but we eliminate it because it will allow us to retain a considerably larger amount of peak observations in our analysis.

The remaining variables are selected based on a combination of statistical significance and predictive power. The initially retained variables for modeling log-surge are: temperature (mean and median), precipitation (maximum, mean, median, and summed), mean snow depth, mean SWE, log of baseflow, latitude, and

longitude. To validate the accuracy of our GAM, we implement 10-fold cross-validation at the streamgage, rather than observation, level. We track GAM results from both including and excluding snow depth so see if a simplified model will yield similar results. The results from this initial GAM are given in Table 5, with mean squared error (MSE) and mean absolute error (MAE) resulting from 10-fold cross-validation. These results show that the model containing snow depth performs slightly better, but the amount of observations the model is able to utilize is more limited due to large amounts of missing snow depth values.

Table 5: Initial GAM accuracies, both including and excluding snow depth.

GAM Formula	**Exp. Deviance**	R^2	**MSE**	**MAE**	**Obs. Utilization**
Without Snow Depth	75%	0.75	0.83	0.48	6,675
With Snow Depth	76%	0.76	0.94	0.49	5,143

To assess the effectiveness of the GAMs in surge representation, we observe the performance of a null model to compare with the accuracy of the GAM predictions. This model does not contain explanatory or response variables—it simply uses the global median of the log of surge multiplier we are predicting with the GAMs. After 10-fold cross-validation, this basic model produces a MSE of 3.28 and a MAE of 0.8. Since the fitted GAM excluding snow depth reduces the MSE by 75% and the MAE by 40% and the GAM containing snow depth reduces MSE by 71% and MAE by 38% relative to the null model, we have evidence to the support that both GAMs produce meaningful predictions and we proceed to further tune them to improve their accuracy.

GAM models with less variables are easier to deploy and less sensitive to small changes in the input data. This motivates us to narrow the model formula down to include just one temperature and one precipitation measurement type. We then fit GAMs with each formula from this list to determine which has the smallest MSE after cross-validation. Lists of MSEs resulting from each precipitation and temperature variable combination for the model with snow depth and the model without are given in Table 6 and Table 7, with the most accurate temperature/precipitation combination highlighted in red in the top row. The best variable combination turns out to be the same for the GAMs both including and excluding snow depth, the exception being that the GAM containing snow depth uses mean snow depth in addition to the following variables: median temperature, maximum precipitation, mean SWE, log of baseflow, and geographic location.

Table 6: Without snow depth: MSEs of all combinations of temperature and precipitation summary statistics when included as variables in the GAM. Additional explanatory variables in each GAM model that are not varied are mean SWE (unique to each peak), log of baseflow, latitude, and longitude. The red text identifies the most accurate variable combination.

Temperature	**Precipitation**	**MSE**	R^2
Median	Max	0.83	0.75
Mean	Max	0.83	0.75
Median	Sum	0.84	0.74
Median	Mean	0.85	0.74
Mean	Sum	0.85	0.74
Mean	Mean	0.85	0.74
Median	Median	0.92	0.72
Mean	Median	0.92	0.72

In order to introduce the mathematical formulation of the simplified GAMs, let $\boldsymbol{u}$ and $\boldsymbol{v}$ be vectors representing a collection of one or more geographic coordinates, in (longitude, latitude) format. Further, let $\boldsymbol{u}$ correspond to the geographic location of the streamgage measuring the i^{th} surge and $\boldsymbol{v_j}$ correspond to the unique geographic locations of the j SNOTEL stations located in the same HUC region as the related streamgage. Recall from the previous section that temperature, snow depth, precipitation, and SWE measurements are calculated by taking the median of the means over the five days prior to peak occurrence of the daily measurements reported at each SNOTEL station contained in the same HUC region as the streamgage where the peak occurred.

Let $\bar{\boldsymbol{t}}$ be the vector of length j containing mean temperature measurements at multiple SNOTEL stations (with locations $\boldsymbol{v_j}$) for the 5 days prior to peak occurrence in the relevant HUC region (k_α). Since there

Table 7: With snow depth: MSEs of all combinations of temperature and precipitation summary statistics when included as variables in the GAM. Additional explanatory variables in each GAM model that are not varied are mean SWE (unique to each peak), log of baseflow, latitude, and longitude. The red text identifies the most accurate variable combination.

Temperature	Precipitation	MSE	R^2
Median	Max	0.93	0.76
Mean	Max	0.94	0.76
Median	Sum	0.94	0.75
Median	Mean	0.94	0.75
Mean	Sum	0.95	0.75
Mean	Mean	0.95	0.75
Median	Median	1.02	0.74
Mean	Median	1.03	0.74

are often multiple SNOTEL stations within a HUC region, we summarize over k_α by finding the median, represented by the superscript (m), of the mean temperature measurements from all j SNOTEL stations. Finally, let i indicate the index of the surge in our data frame of flood peaks that this value is calculated for. Thus, we have

$$\bar{\boldsymbol{t}}^{(m)}(\boldsymbol{v_j} \in k_\alpha)_i,$$

which represents the calculation made to determine the measurement for mean temperature at each surge. We use similar notation for mean SWE ($\bar{\boldsymbol{s}}_{\boldsymbol{w}}$), mean snow depth ($\bar{\boldsymbol{s}}_{\boldsymbol{d}}$), and maximum precipitation ($\boldsymbol{p_{max}}$). The remaining explanatory variables, baseflow (b_f) and the geographic location of the gage ($\boldsymbol{u}$), are derived from streamgage rather than SNOTEL stations, and require no statistical summary prior to inclusion in the model.

Let $f_1 \dots f_5$ denote the default smoothing functions used in our model that employ penalized thin plate regression splines, as described by Wood (2003). These penalized splines allow us to control both the smoothness of the fitted splines while maximizing their accuracy through leave one out cross-validation. Additionally, let h represent the smoothing function applied to the geographic coordinates composing the model's spatial element. h employs isotropic second order splines on the sphere, which are analogous to thin plate regression splines but for a spherical environment (Wendelberger, 1982). The finalized GAM formula containing snow depth and including the smoothing functions applied to the combination of explanatory variables to predict the log of surge (g) is given in Equation 4.

$$\begin{aligned} \log\left[g(\boldsymbol{u} \in k_\alpha)_i\right] = f_1\left[\boldsymbol{t}^{(m)}_{\boldsymbol{med}}(\boldsymbol{v_j} \in k_\alpha)_i\right] + f_2\left[\boldsymbol{p}^{(m)}_{\boldsymbol{max}}(\boldsymbol{v_j} \in k_\alpha)_i\right] \\ + f_3\left[\bar{\boldsymbol{s}}^{(m)}_{\boldsymbol{w}}(\boldsymbol{v_j} \in k_\alpha)_i\right] + f_4\left[\bar{\boldsymbol{s}}^{(m)}_{\boldsymbol{d}}(\boldsymbol{v_j} \in k_\alpha)_i\right] + \\ + f_5\left[\log b_f(\boldsymbol{u} \in k_\alpha)_i\right] + h\left[(\boldsymbol{u} \in k_\alpha)_i\right] + \epsilon. \end{aligned} \tag{4}$$

The formula for the GAM excluding snow depth is equivalent to Equation 4 but with the snow depth term removed.

Station Profiles

The primary purpose of the GAM models is to quantify changes in predicted stream surge for different combinations of variables representing ROS and non-ROS events. Using the final two GAM models, we formulate characteristic profiles for ROS and non-ROS conditions specific to each streamgage. We do this by using the summary statistics shown in Table 8 for each explanatory variable utilized in our GAM. The median annual maximum is chosen in several cases to represent what would be considered an "extreme" ROS event, as it is likely that the snowpack will not be at its peak when a ROS event occurs. In this way, the profile is intended to provide a conservative estimate of the relative difference between ROS and non-ROS induced stream surge. A more detailed description of why we choose each specific summary statistic to represent the profiles is given below Table 8.

Table 8: Values used to describe characteristic profiles for ROS and non-ROS events.

Variable	ROS	Non-ROS
Temperature	overall ROS median	overall non-ROS median
Snow depth	median annual maximum	0
Precipitation	median annual maximum	median annual maximum
SWE	median annual maximum	0
Baseflow	overall median	overall median
Location	station-specific	station-specific

- **Temperature:** We use the global medians of non-ROS and ROS classified peaks, since measurements for both scenarios remain somewhat consistent across locations. Unlike other variables, these values are set globally, rather than separately for each station.
- **Precipitation:** We use the median annual maximum precipitation measurement for both non-ROS and ROS induced peaks because current engineering design practice relies on projections of extreme precipitation that does not discriminate between ROS and non-ROS events.
- **Snow Depth:** We use a measurement of zero for non-ROS induced peaks because a ROS event cannot occur if there is no snow. We then use the median annual maximum snow depth measurement for ROS induced peaks because it is representative of a large, though not uncommon, snow accumulation event.
- **SWE:** We use a measurement of zero for non-ROS induced peaks and the median annual maximum SWE for ROS induced peaks, using the same justification that we use for snow depth.
- **Baseflow:** We use the median overall baseflow measurement for each streamgage, as it gives of a sense of the typical flow at the gage.

To reiterate, we hold precipitation and baseflow constant for both ROS and non-ROS conditions, while allowing SWE and temperature to vary between surge type.

Training the GAMs

With the profiles compiled for each streamgage, we train the GAMs on the original data containing information about each peak before predicting onto the dataset containing only the characteristic profiles for each streamgage. After generating predictions for both the non-ROS and ROS profiles at each streamgage, we calculate the ratio between ROS and non-ROS exponentiated surge multipliers, furthermore referred to as the ROS Stream Surge Ratio (ROSSR). The ROSSR is calculated by streamgage similarly to the empirical surge ratios in Equation , but without the aggregation by median, resulting in the following simplified formula:

$$r = \frac{\hat{g}_r}{\hat{g}_n},$$

where r is once again the ratio, $\hat{g}_r$ is the predicted surge for the ROS profile, and $\hat{g}_n$ is the predicted surge for the non-ROS profile. The distributions of these ratios from the GAMs both including and excluding snow depth are used to investigate the general behavior of surges in ROS vs non-ROS flood peaks, as shown in Figure 19. We see that the GAM excluding snow depth generates surge predictions for ROS and non-ROS that are more similar to each other than those produced by the GAM containing snow depth.

To better understand the role each term in Equation 4 plays in the predicted surge values, we examine plots of the marginal effects for both GAMs. Starting with the GAM including snow depth, we see from Figure 20 that the variable with the largest effect on predicted surge is baseflow. This is likely because baseflow is the denominator of surge (see Equation 1), so higher values produce lower predictions. Precipitation is positively associated with predicted surge, though the effect size is small in comparison with baseflow. Temperature produces its highest effect size between zero and ten degrees, trending up again as it approaches 40°C. Snow depth and SWE do not appear to contribute as much to the predictions relative the other variables. They also appear to have counteractive effects, with snow depth being positively associated with surge and SWE being negatively associated.

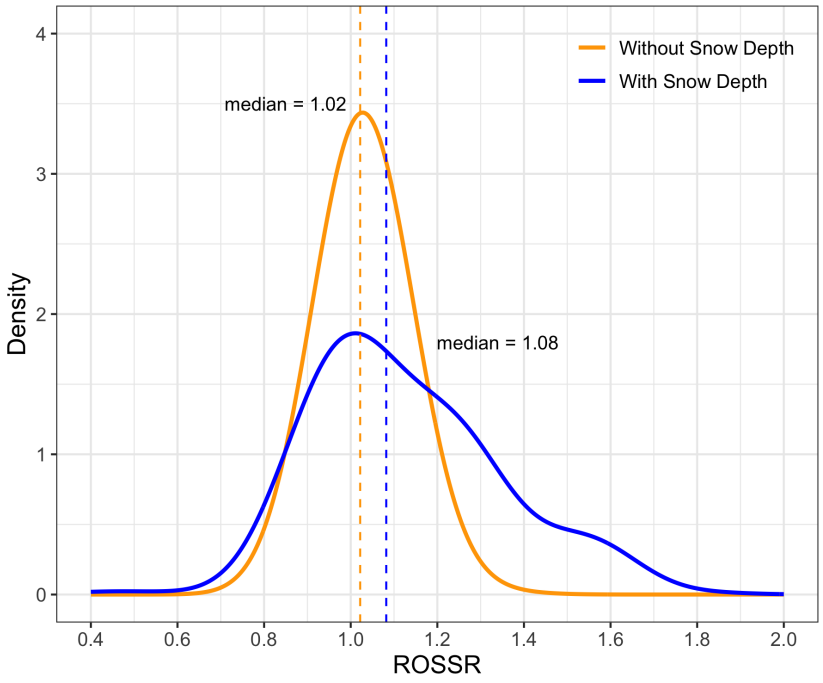

Figure 19: Distribution of ratios of surge predictions for ROS and non-ROS behavior at streamgages with qualifying peaks for both the GAM with snow depth and the GAM without.

Figure 21 uses local scales for the y-axis of each marginal effect, which highlights trends that are not clearly visible in Figure 20. Here we see slight positive and negative trends in snow depth and SWE, respectively.

Figure 22 shows the marginal effect of the spatial term included in the GAM. It shows that, after accounting for the effects contributed by all other variables, the gages located in the southern and eastern parts of the region of interest tend to have slightly larger stream surges. We postulate that the purpose of this trend is to smooth out differences between areas with high and low water flows, but future work should investigate the reasons for these spatial patterns.

Figures 23-25 show marginal numeric and spatial effects for the GAM excluding snow depth, with most variables producing similar contributions to those previously discussed for the GAM including snow depth. Note that the relationship between SWE and predicted surge is non-linear, though the association does not appear to be significant based on the standard errors of the marginal effect. The model calculates a p-value of 0.015, indicating that the SWE effect is marginally significant.

We use bootstrapping techniques to investigate the sensitivity of the median ROSSRs shown in Figure 19. To do this, we generate predictions for 200 bootstrap samples and use them to approximate the distribution of the median r from each sample. The distributions of these medians are shown in Figure 26 for both GAMs. We observe that the model containing snow depth has notably more sensitivity/variability than the model excluding it. There is little visual evidence to suggest that the medians of either of these distributions are much different from 1.0, though the empirical results suggest that the values do tend to be higher (by 3-9%) when including large SWE values in the prediction, but the results are highly variable and likely not statistically significant.

To illustrate the sensitivity of the GAM projections to changes in ROS, Figure 27 also includes curves showing the ROSSR if the quantity for snow depth and SWE in the characteristic profiles were cut in half (for both the models including and excluding snow depth). Medians for both distributions increase substantially and variability decreases. There is strong visual evidence that the medians of both distributions are significantly above 1.0 after halving the snow accumulation profile. With these smaller SWE values, the models predict that surges will be 9-20% larger for a ROS event as opposed to a non-ROS event.

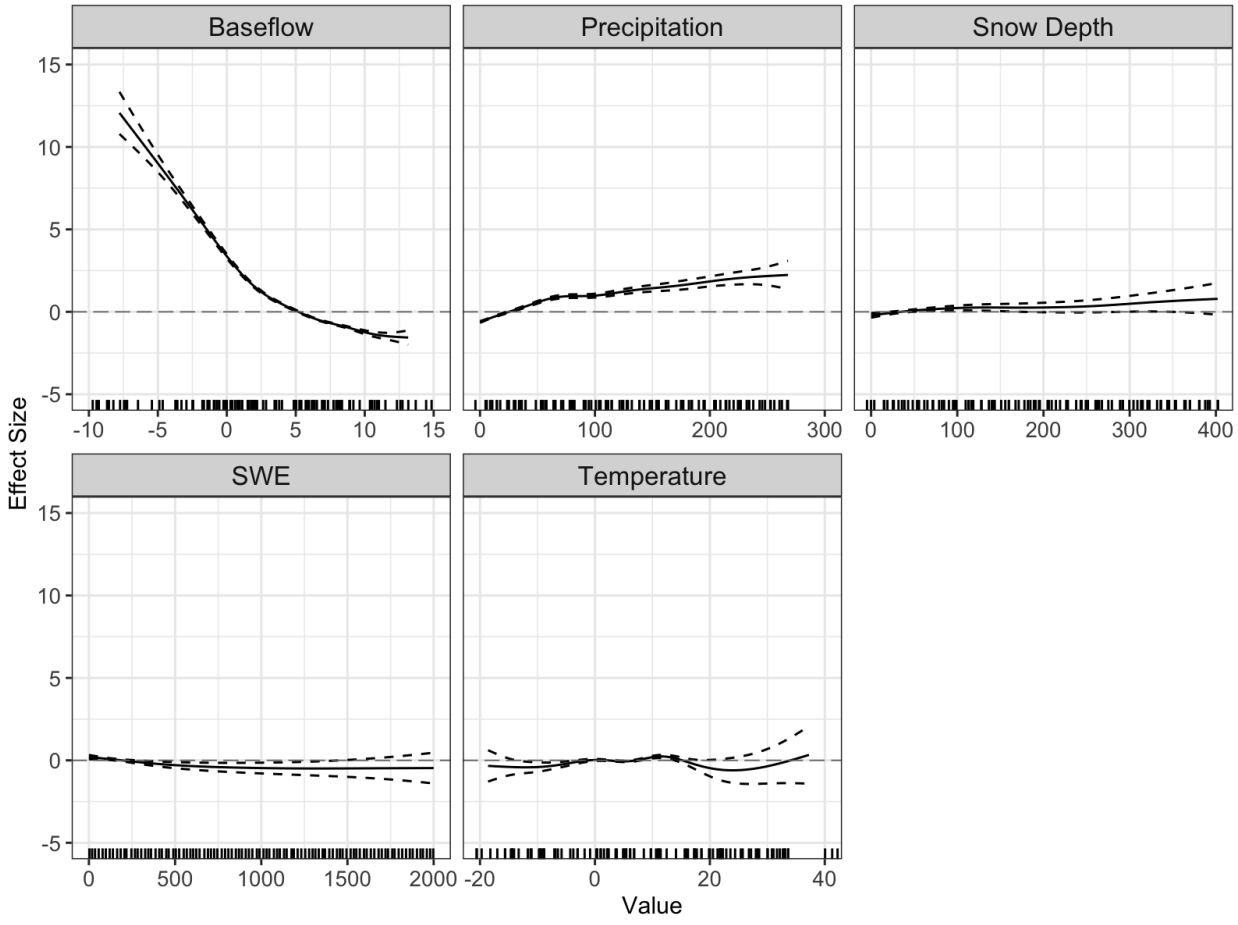

Figure 20: Marginal effects of numeric variables included in the GAM with snow depth with fixed vertical axes. Effect size is shown in addition to margin of error and rug plots along the horizontal axes.

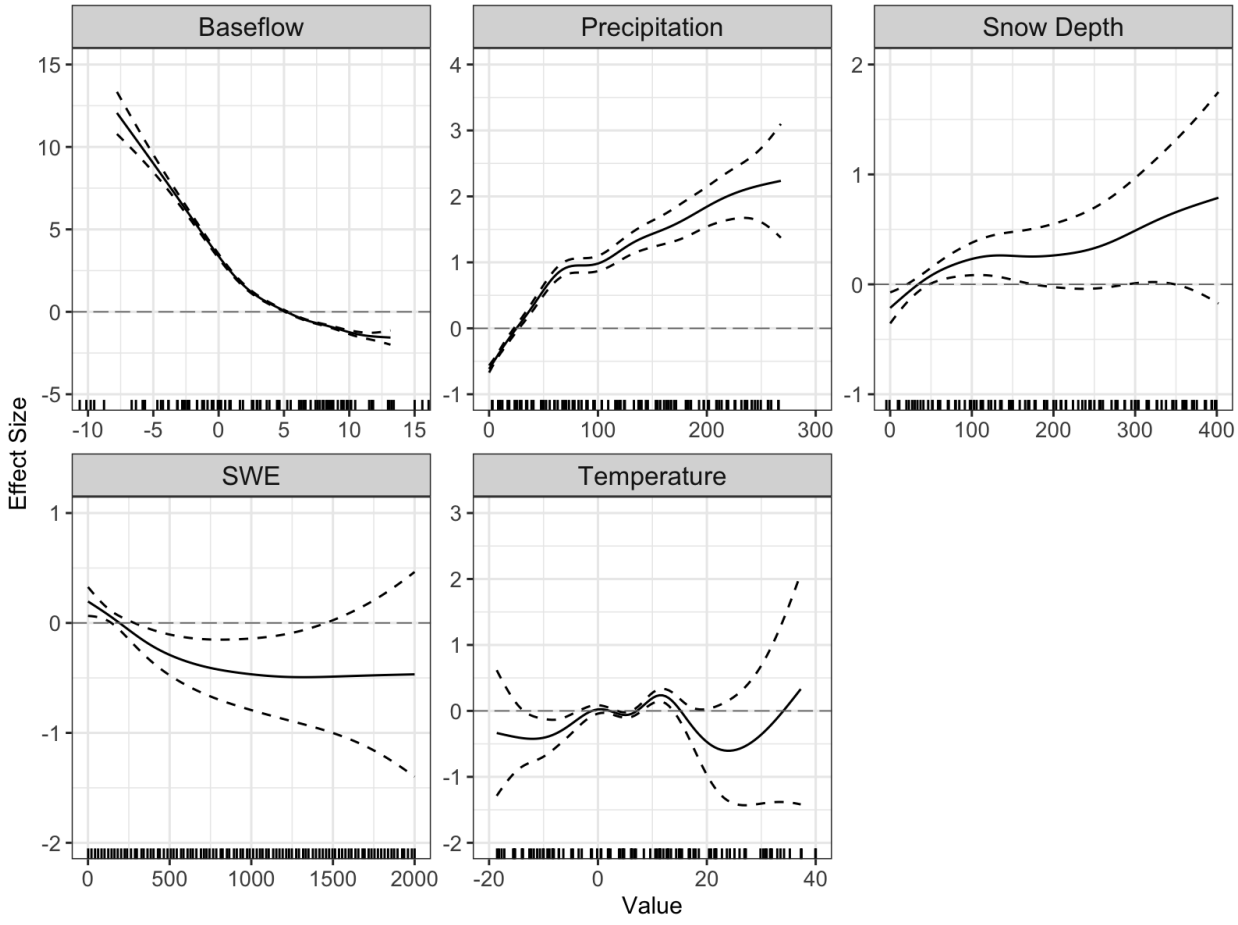

Figure 21: Marginal effects of numeric variables included in the GAM with snow depth with varying vertical axes. Effect size is shown in addition to margin of error and rug plots along the horizontal axes.

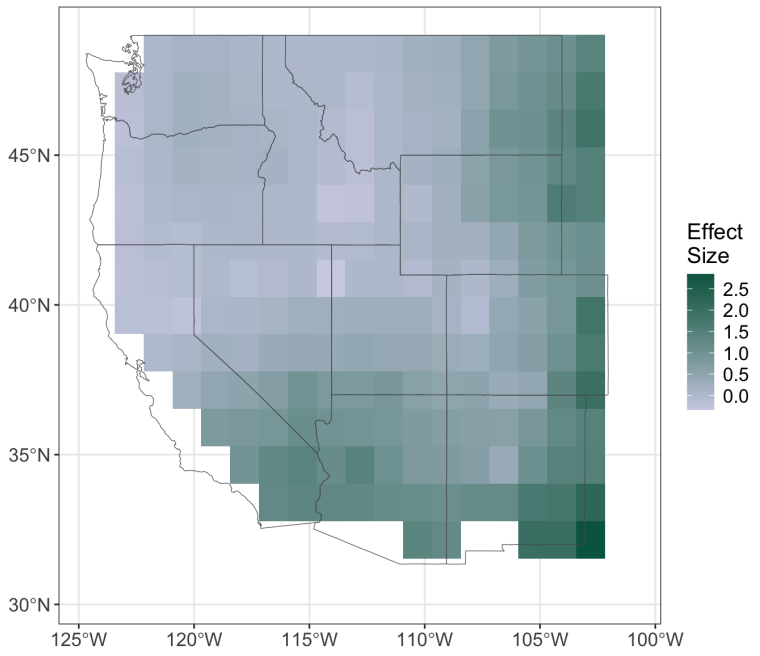

Figure 22: Marginal effect of spatial term in the GAM containing snow depth.

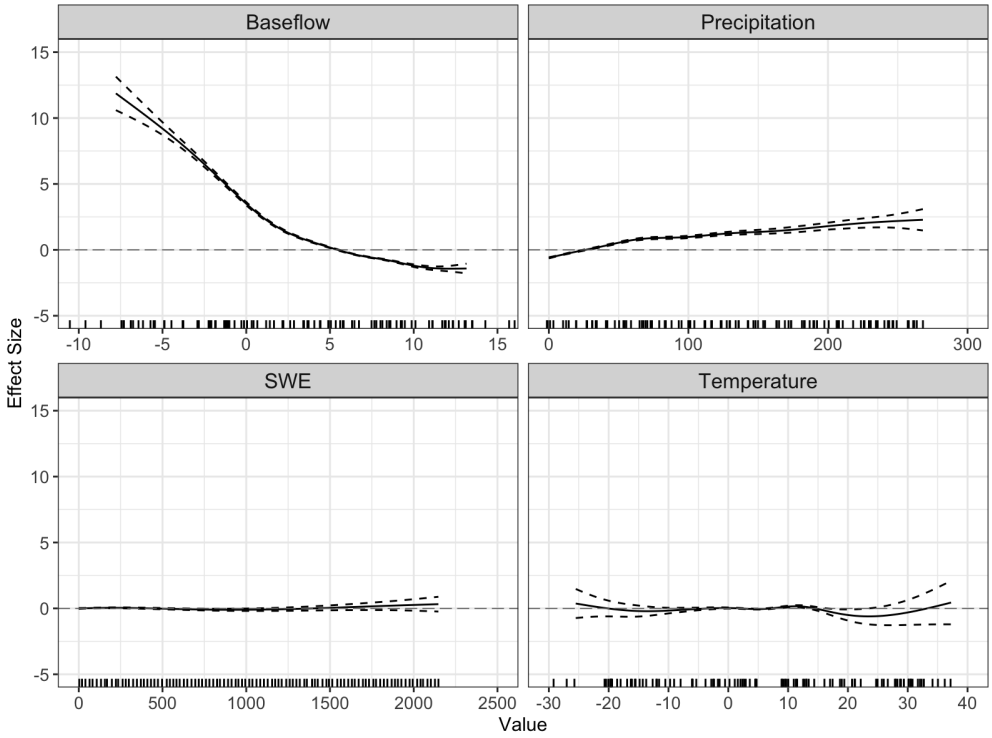

Figure 23: Marginal effects of numeric variables included in the GAM without snow depth with fixed vertical axes. Effect size is shown in addition to margin of error and rug plots along the horizontal axes.

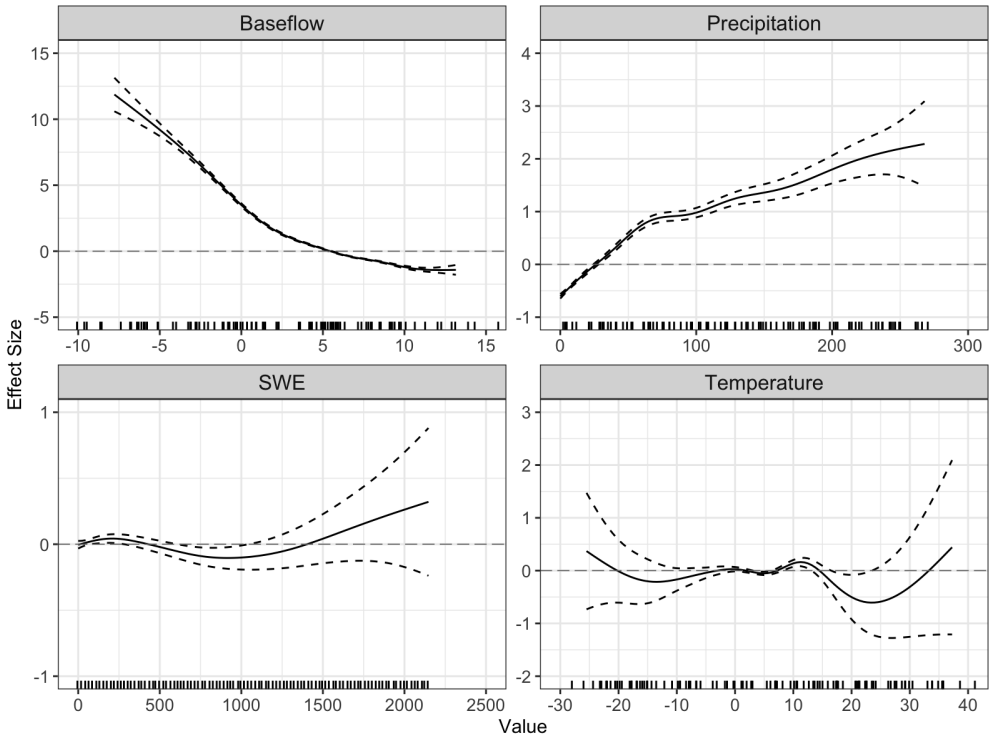

Figure 24: Marginal effects of numeric variables included in the GAM without snow depth with varying vertical axes. Effect size is shown in addition to margin of error and rug plots along the horizontal axes.

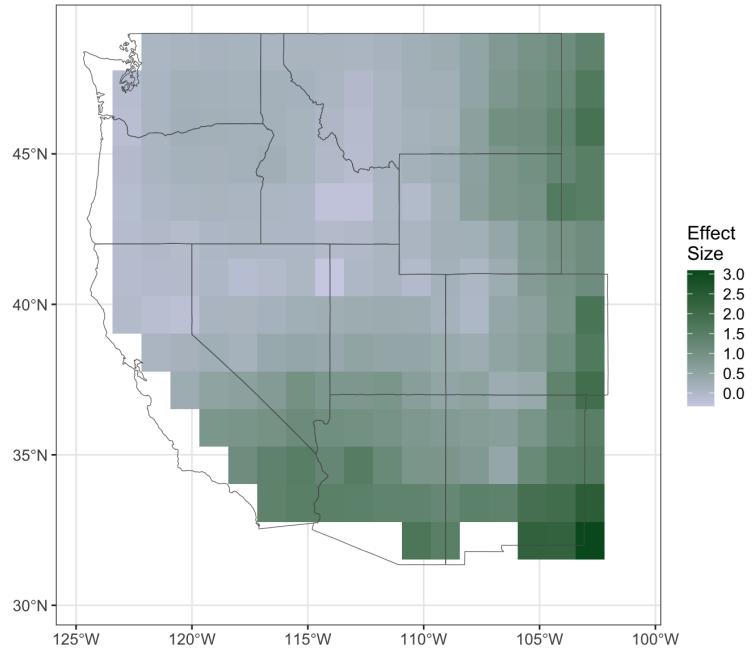

Figure 25: Marginal effect of spatial term on the GAM excluding snow depth.

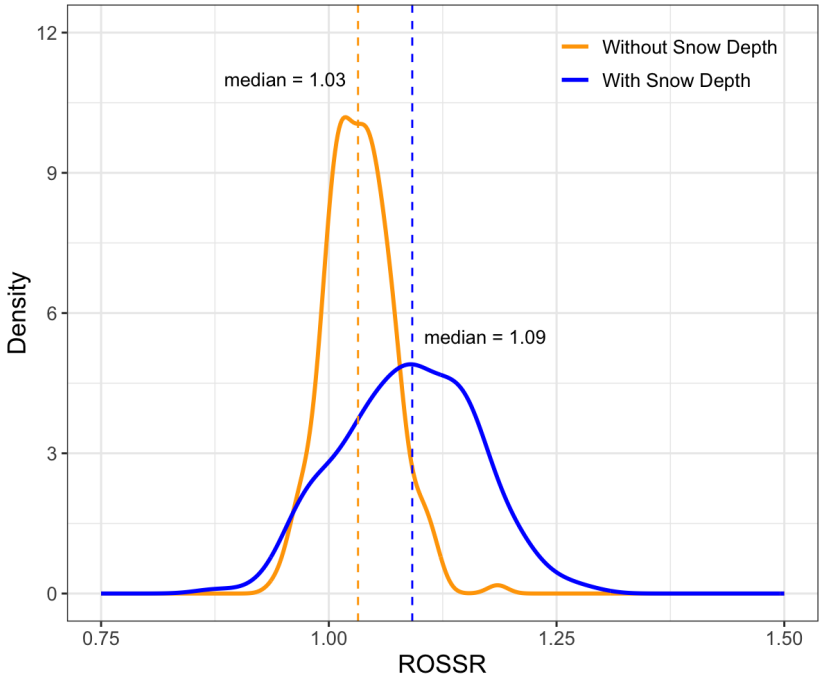

Figure 26: Distribution of bootstrapped median ROSSR for both the GAM with snow depth and the GAM without.

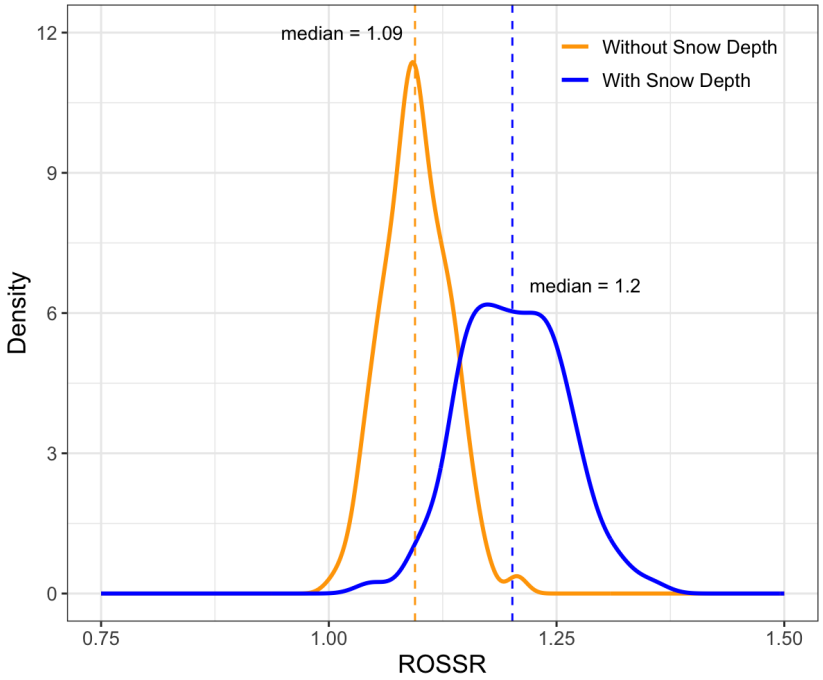

Figure 27: Distribution of ratios of surge predictions for ROS and non-ROS behavior at streamgages with qualifying peaks for both the model with snow depth and the model without with halved SWE and snow depth profile values.

Overall Figures 26-27 show that **the relative difference between a median ROS and median non-ROS stream surge prediction is about 3-20% larger depending upon the selected model.** This result is in line with the 1.16 ratio obtained in the GAM model that included snow depth measurements and subsequently used in the culvert design examples provided as part of this report. The sensitivity of the predicted relative different warrants additional explorations beyond the timeline allocated for this study. **That in mind, in the spirit of engineering conservatism, we recommend that NDOT consider a 10-15% bump in their HEC-HMS flow values in regions of Nevada where ROS has historically been an issue.**

Design Implications

The previous section describes a recommended 1.15 multiplier on design flows to account for the flow surcharge due to a ROS event. In this section, we consider the implications of incorporating such a surcharge into culvert design. Note that the results in this section explore the implications of using multipliers of 1.16, 1.33 and 2.15. These candidate multipliers came from a preliminary version of Figure 19 and represented the median, 75th percentile, and maximum ROSSR from that preliminary model (which included snow depth). The final model, which included more data points, had slightly reduced values for each of these multipliers. Nevertheless, the design examples shown in this section are still representative of the implications of a moderate (1.16 and 1.33) and extreme (2.15) change in design flows to respond to the potential threat of ROS. All this in mind, we note that the median multiplier (then 1.16, now 1.10 to 1.15) is a more robust estimate of ROSSR than the higher multipliers which are sensitive to changes in the input data.

Per communications with NDOT, the research team performed culvert designs using the HY-8 culvert design software (FHWA, 2022) and the NDOT Drainage Manual (NDOT, 2006) to analyze over five hundred culvert design scenarios, exploring the use of the surge factors applied to the flows (Q) of two sites. The team generated the ".hy8" files using an MS Excel macro spreadsheet to speed up the process, which included generating different culvert lengths and crest heights while maintaining the other parameters constant. Table 9 shows the variables explored in this study, which included the two sites shown in Figure 28 with their respective flows, two surge factors, two culvert materials, two culvert sections for concrete and one for metal, three culvert lengths, crest heights, and slopes, and two inlet treatments. The selected inlet treatments correspond to extreme values for the available options in HY-8 that produce inlet entrance coefficients, K_e, of 0.70 and 0.20. For example, for circular shapes, this selection corresponded to the "Mitered to Conform to Slope ($K_e = 0.7$)" and "Beveled Edge (1:1) ($K_e = 0.20$)" options, while for the concrete box, the designs used "Square Edge (0° flare) Wingwall ($K_e = 0.7$)" and "1:1 Bevel Headwall ($K_e = 0.2$)" options in the software.

Table 9: Parameters used in the study to examine the effects of surge factors on the dimensions of round and square culverts.

Name	**Type**	**Cases**	**Value #1**	**Value #2**	**Value #3**
Location	Site	2	Carson City	US6 East of Tonopah*	-
Flow	Q	2	11 cfs	610 cfs	-
Surge Factor	Multiplier	2	1.00	1.16	1.33 (excluded)
Culvert	Material	2	Concrete	Metal	-
Form	Shape	2	Circular	Box	-
Culvert Length, L	Length	3	20	200	-
Crest Elevation Site 1	Length	3	10 ft	15 ft	20 ft
Crest Elevation Site 2	Length	3	4 ft	8 ft	10 ft
Trail Water Height, TW	Length	2	1 ft (Carson City)	6.3 ft (US6 East of Tonopah)	-
Slope	Percent	3	1%	10%	15%
Inlet treatment	Entrance	2	None	45 deg	-

*- The selection of the US6 East of Tonopah site was a hypothetical case study and does not imply that all factors would be appropriate for the location.

Figure 28: Screenshots showing the locations of the study sites #1 (top) and #2 (bottom). Site #1 is East of Tonopah, while site #2 is in Carson City, between milepost CC-0 and CC-3 of US50.

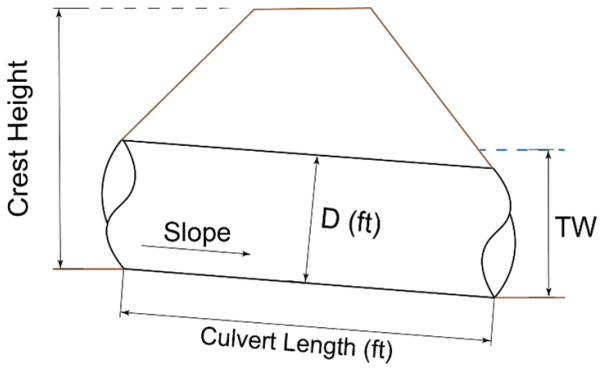

Figure 29: Illustration showing the variables used in the parametric study. The sum of the diameter of the culvert is added to the fill above it to result in the "Crest height" variable.

It is important to note that the study only accounted for the overtopping failure case, disregarding the excessive velocity in the culvert because that is a remediable problem. In addition, the freeboard limit is just below the crest of the road, or 0 ft, which implies no freeboard between the water flow and the crest of the road. This is the most severe culvert design case and was determined in agreement with NDOT. Moreover,

the study did not account for the effect of debris or sedimentation in the culverts, both of which can increase the likelihood of overtopping obstructing the flow.

Design Results

This section provides the results of the parametric study introduced above in terms of culvert dimensions, total headwater, and overtopping flow. The research team selected culvert sizes following ASTM Standards pertaining to the fabrication of metal and concrete culverts (ASTM, 2020, 2021, 2022) to account for commercially available culverts only, making the results more applicable to real designs.. Initial analysis showed a correlation between culvert length and flow velocity in the culvert but no correlation between the headwater and the length, as expected. For example, when designing a circular concrete culvert with a 2% culvert slope, the flow velocity increased from 12 ft/s to 19 ft/s when comparing a 20 ft culvert to a 200 ft one. However, internal treatment can remediate the flow velocity to avoid culvert erosion, and for that reason, this research does not consider the excessive flow velocity as a failure criterion. The authors observed a similar effect when combining the slope with the surge factors, indicating that a culvert size increase is only necessary when internal culvert treatment is impractical. Table 10 shows the results of the culvert design for Site 1 with and without surge factors while implementing a mitered to conform to slope inlet treatment ($K_e = 0.70$). The first two rows of the table display the results for a combination of a short span and a low elevation of the crest, which yielded a 6-ft diameter concrete pipe without a surge factor and a 6.5-ft diameter concrete pipe with a surge factor of 1.16. Other analyses resulted in similar results, indicating that culvert diameters may increase by 0.5 ft if a surge factor of 1.16 was implemented. Nonetheless, when the fill above the culvert is large enough (10-15 ft), the surge factor does not always drive up the culvert size when considering commercial sizes only. Moreover, these cases where the surge factor drove the pipe diameter up may be remediated if the inlet treatment changed from a mitered to conform slope to a beveled edge (1:1), as shown in Table 11. However, if the inlet treatment already had a beveled edge, the retrofit would not be as straightforward as the previous one. It would involve modifying the hydraulic structure's features to avoid overtopping. Appendix A presents the rest of the design scenarios for a slope of 2%. The tables presented herein also exclude two culvert crest elevations in each row due to having identical results when compared to other lengths with similar properties.

Table 10: Results of six culvert designs for site #1 using a circular concrete section, with and without a surge factor of 1.16, an inlet treatment with Ke=0.70, and three different crest elevations. Variables (units) include L (ft), Slope (%), Q (cfs), TW (ft), Crest (ft), D (ft), and HW (ft).

L	Slope	Q	TW	Crest	Inlet Treatment	Barrels	D	HW	Overtopping
20	2%	610	6.3	10	Mitered to Conform to Slope (Ke=0.7)	2	6.0	9.63	628.73
20	2%	708	6.3	10	Mitered to Conform to Slope (Ke=0.7)	2	6.5	9.79	720.01
50	2%	610	6.3	15	Mitered to Conform to Slope (Ke=0.7)	2	5.0	15.02	608.37
50	2%	708	6.3	15	Mitered to Conform to Slope (Ke=0.7)	2	5.5	14.55	722.67
200	2%	610	6.3	20	Mitered to Conform to Slope (Ke=0.7)	2	5.0	15.06	720.06
200	2%	708	6.3	20	Mitered to Conform to Slope (Ke=0.7)	2	5.0	19.4	720.06

Table 11: Results of six culvert designs for site #1 using a circular concrete section, with and without a surge factor of 1.16, an inlet treatment with Ke=0.20, and three different crest elevations.

L	Slope	Q	TW	Crest	Inlet Treatment	Barrels	D	HW	Overtopping
20	2%	610	6.3	10	Beveled Edge (1:1) (Ke=0.20)	2	5.5	9.48	636.36
20	2%	708	6.3	10	Beveled Edge (1:1) (Ke=0.20)	2	6.0	9.52	737.41
50	2%	610	6.3	15	Beveled Edge (1:1) (Ke=0.20)	2	5.0	11.81	721.3
50	2%	708	6.3	15	Beveled Edge (1:1) (Ke=0.20)	2	5.0	14.59	721.29
200	2%	610	6.3	20	Beveled Edge (1:1) (Ke=0.20)	2	4.5	15.88	696.23
200	2%	708	6.3	20	Beveled Edge (1:1) (Ke=0.20)	2	5.0	14.59	853.47

Table 12 shows the results of designing culverts for site #2, where the flow is small compared to the one in site #1. The first two rows of the table show the design for the smallest crest elevation in the set of culvert designs, considering a non-interstate case with a minimum internal pipe diameter of 18 inches. For that case and the following cases, the resulting diameter satisfies both designs with and without a surge factor, indicating that for low flows, the surge factor of 1.16 may not increase the culvert size because the culvert overtopping flow is nearly 100% larger than the magnified flow. Moreover, using an inlet treatment other than the mitered to conform slope would also decrease the likelihood of overtopping for the low flow due to decreasing the required culvert diameter to the minimum stipulated by the NDOT drainage manual. Similar results are obtained when using circular metal pipes and are presented in Appendix B along with other design scenarios.

Table 12: Results of six culvert designs for site #2 using concrete circular pipes, with and without a surge factor of 1.16, inlet treatment with Ke=0.70, and three different crest elevations.

L	Slope	Q	TW	Crest	Inlet Treatment	Barrels	D	HW	Overtopping
20	2	11.0	1	4	Mitered to Conform to Slope (Ke=0.7)	1	1.75	2.96	18.24
20	2	12.8	1	4	Mitered to Conform to Slope (Ke=0.7)	1	–	–	–
50	2	11.0	1	8	Mitered to Conform to Slope (Ke=0.7)	1	1.5	2.9	20.86
50	2	12.8	1	8	Mitered to Conform to Slope (Ke=0.7)	1	–	–	–
200	2	11.0	1	10	Mitered to Conform to Slope (Ke=0.7)	1	1.5	2.9	22.45
200	2	12.8	1	10	Mitered to Conform to Slope (Ke=0.7)	1	–	–	–

Design Conclusions

This section presented the results of culvert design using a surge factor of 1.16 and 1.00 (current status). All culvert designs were performed in HY-8 using commercially available culvert sizes and data provided by NDOT. Based on the results presented above and in Appendix B, the following conclusions can be made:

- The 1.16 surge factor increases the culvert size by 6"-12" in most cases.
- The surge factor also increases the minimum culvert size from 18" to 21" for sites with low crest heights, measured from the bottom of the inlet to the top of the road.
- For sites with small flows and large crest heights, only the 2.15 surge factor drives up the size of the culvert.
- For sites with large flows and any crest height, factors greater than or equal to 1.16 drive up the size of the culvert in almost all cases.
- Length and slope parameters do not affect the results in terms of overtopping, but they increase the flow velocity. Therefore, culverts with slopes larger than 2% or lengths longer than 100 ft would likely need energy dissipation devices to counteract the effect of the surge factors on the flow.

Utah Climate Center Website

This report has illustrated that the difference between ROS and non-ROS induced snow surge is highly variable, with the typical stream surge from ROS and non-ROS events being nearly identical after controlling for other weather conditions. That in mind, there is still evidence, as highlighted in the examples set forth in the Nevada Decision Support sections, that the most extreme flood events in western Nevada tend to be ROS-induced. In this subsection, we describe efforts by USU's Utah Climate Center to embed an adaptation of the decision support framework described in this report into a forecasting application run daily and hosted by the Utah Climate Center. This website can be found at `https://climate.usu.edu/nvros`, though the launch of this website will not occur until October 2024 to coincide with the start of the first snow season after the completion of this project.

The website uses gridded snow data from SNODAS (NSIDC, 2024) and gridded temperature and precipitation forecasts from the NAM CONUS Hires forecast model (NOAA, 2024). The tool works by inferring the daily amount and density of the snowpack using SNODAS's SWE and snow depth estimates. The model then assumes that the snowpack remains fixed and explores the TWI and runoff potential in 3 hour increments up to 60 hours in the future at a 3km resolution. The colors on the map represent the same colors and thresholds described in the decision support sections of this report. We recognize that the snowpack will continue to evolve as a function of the temperature and precipitation during the forecast period. However, forecasting changes in the snowpack falls beyond the scope of this current effort. In spite of this shortcoming, the website provides a reasonable forecast of ROS potential a few days into the future, which can be used a way to identify areas of Nevada with the potential for runoff-inducing ROS.

Conclusions and Suggested Research

We expanded on the work of Heggli et al. (2022) and integrate the data methods for the Upper Carson to asses and further calibrate the present weather and antecedent snowpack conditions that produce TWI and connect the data to CNRFC hydrologic forecast points in the Upper Carson River Watershed. We assessed an operational approach for the SR-DSS by applying data subjected only to automated quality control routines and applied the SR-DSS to an event that was not included in the development of thresholds. The case study highlights how complicated the snowpack runoff process is as each elevation brings a different combination of antecedent conditions and present weather impacts. However, our research found that precipitation at 0.4 °C can produce TWI within two hours and further proves that the snowpack does not need to reach a certain density to be able to produce TWI. This paper not only advances the development of SR-DSS to serve an unmet need but also improves the understanding of ROS runoff process. Integrating hourly SNOTEL data

provides insight into lag-rates on rainwater moving through the snowpack, snowmelt during ROS, and the total duration of TWI during ROS. Observing patterns of ROS events and connecting those patterns to streamflow provides valuable insights for flood forecasting and management in the Upper Carson watershed.

We have also created a database of stream surge measurements and their antecedent climate conditions. We classified these stream surges as ROS and non ROS-induced and compared differences in relative surge amounts between both groups. These ratios were plagued by a few outlier values, but the results consistently showed that ROS tended to be 3-20% larger than non-ROS events after controlling for station location and stream baseflow. The result is a recommendation of a 1.15 multiplier to provide a conservative adjustment to design flows obtained from HEC-HMS in areas where ROS is expected to be a concern. The implications of such a ratio were further explored in design examples provided as part of this report.

Taken together, the three main components of this report (i.e., Nevada Decision Support, Western State Explorations, and Design Examples), provides important insight into the influence of ROS on Nevada highway design at widely varying spatial and temporal scales. The software, data, and design examples associated with this report provide a solid framework for exploring the engineering design implications related to ROS, which the authors hope will be further explored in future studies by NDOT and other agencies.

Appendix A

SNOTEL Visuals

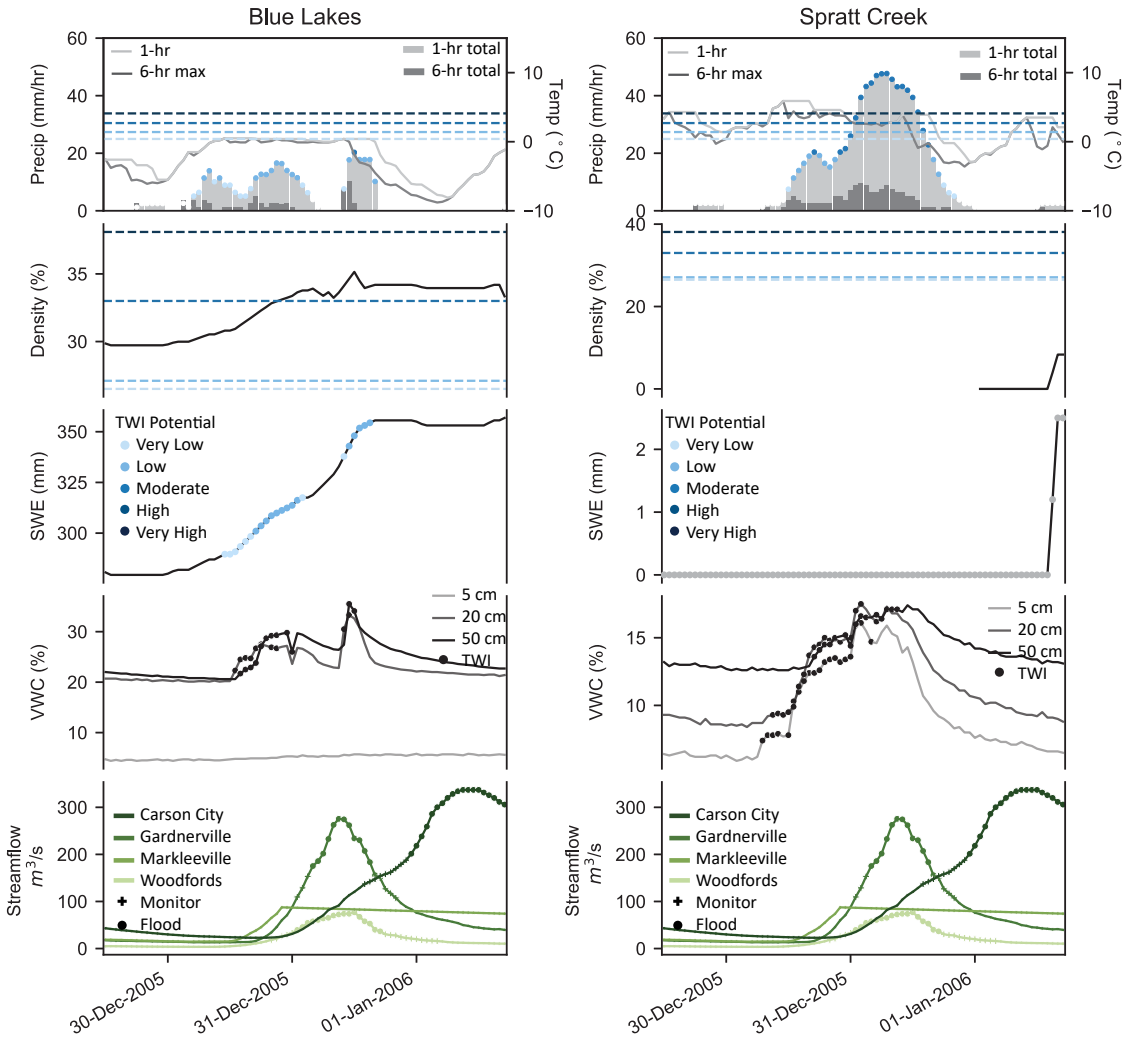

Figure A.1: SR-DSS event assessment: 30 December 2005 – 1 January 2006

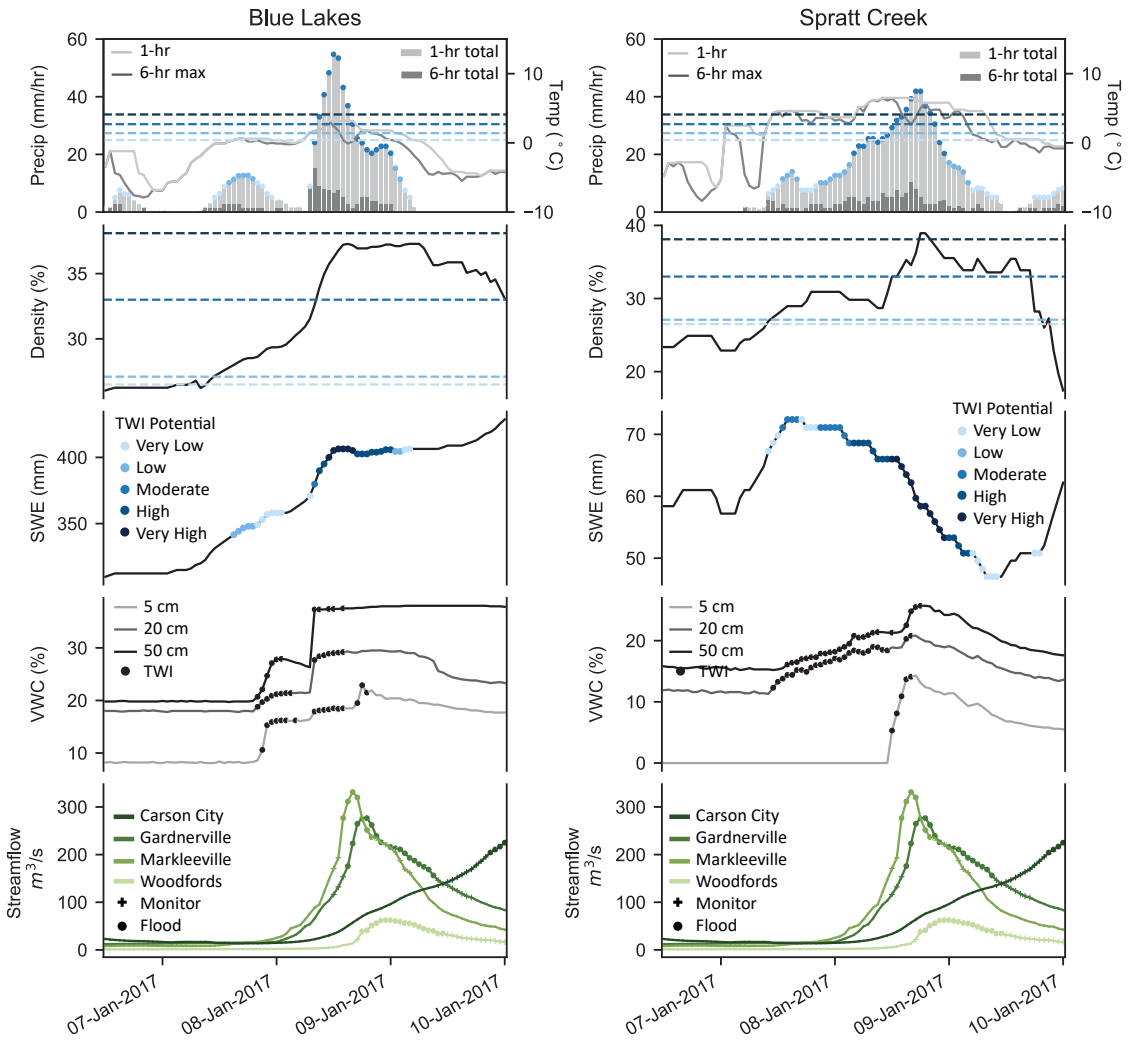

Figure A.2: SR-DSS event assessment: 7 – 10 January 2017

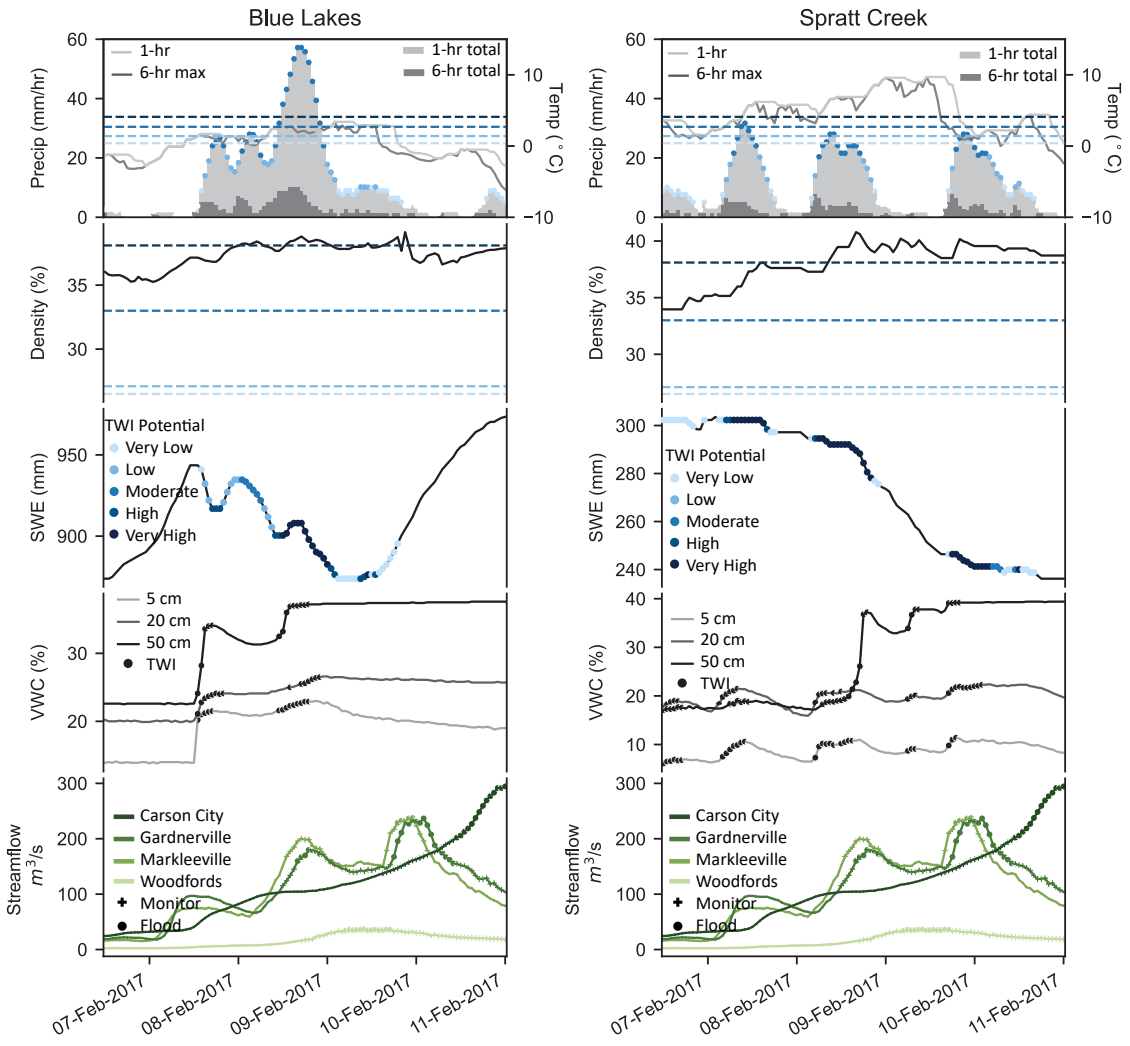

Figure A.3: SR-DSS event assessment: 7 – 11 February 2017

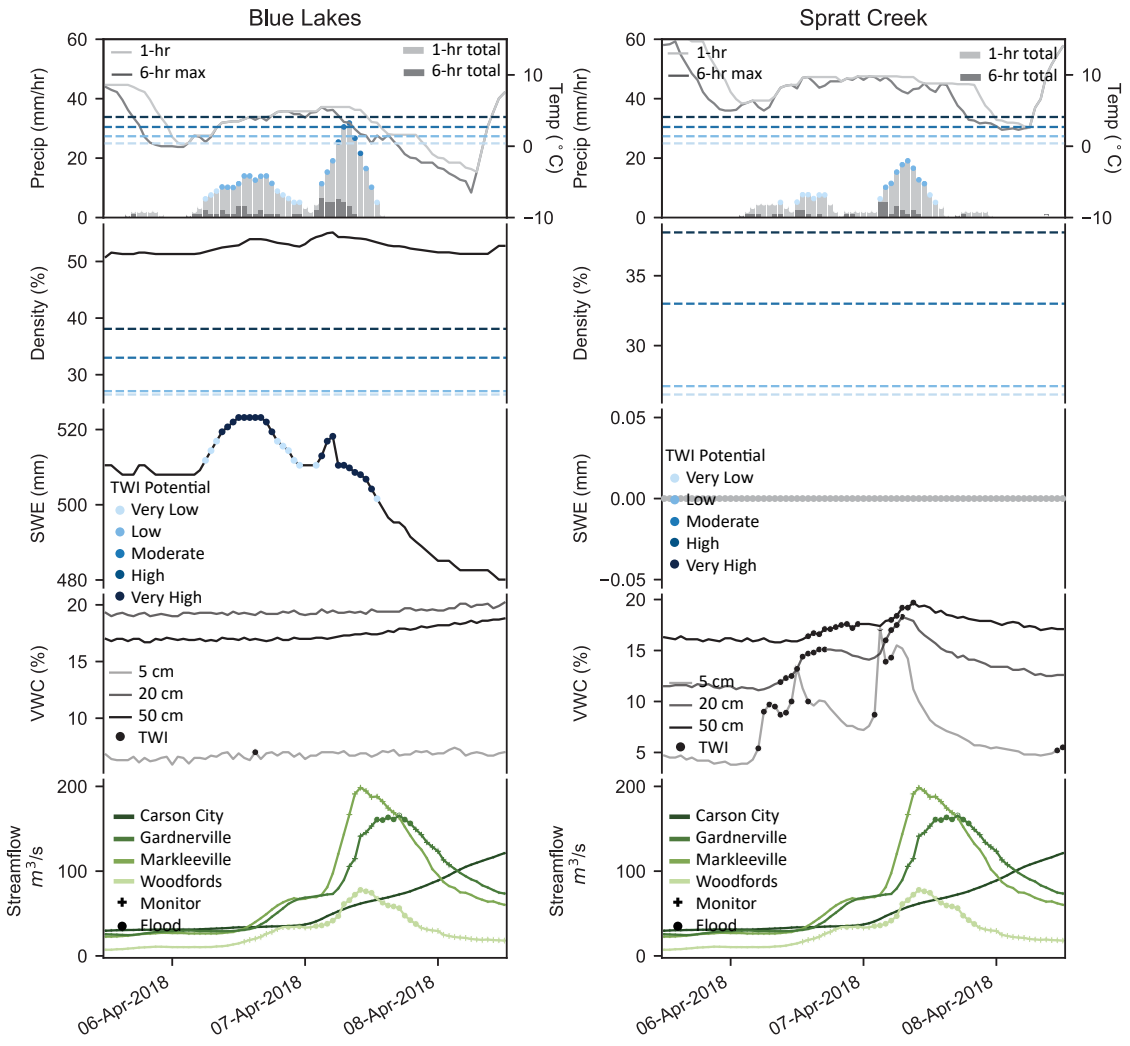

Figure A.4: SR-DSS event assessment: 6 – 8 April 2018

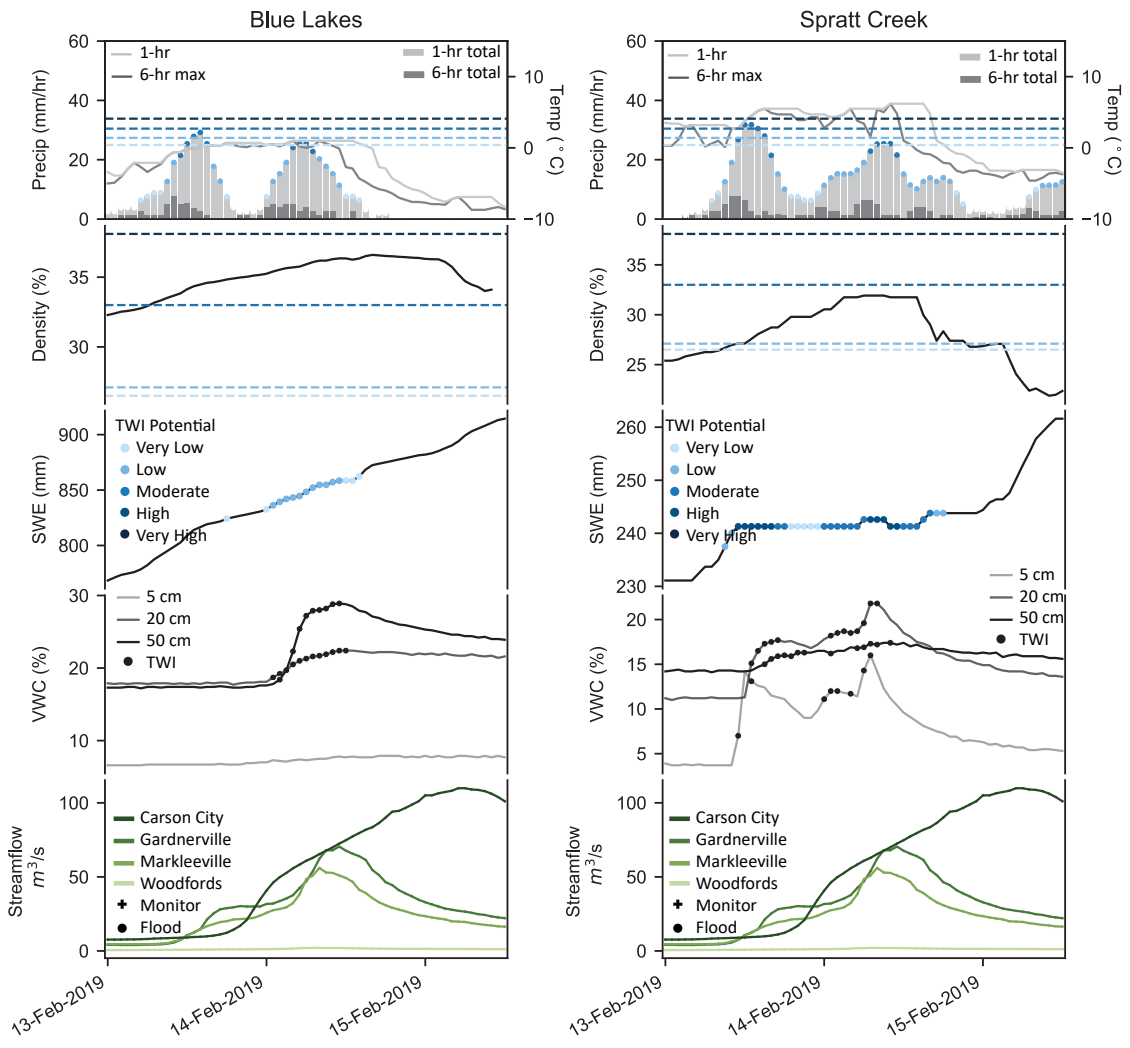

Figure A.5: SR-DSS event assessment: 13 – 15 February 2019

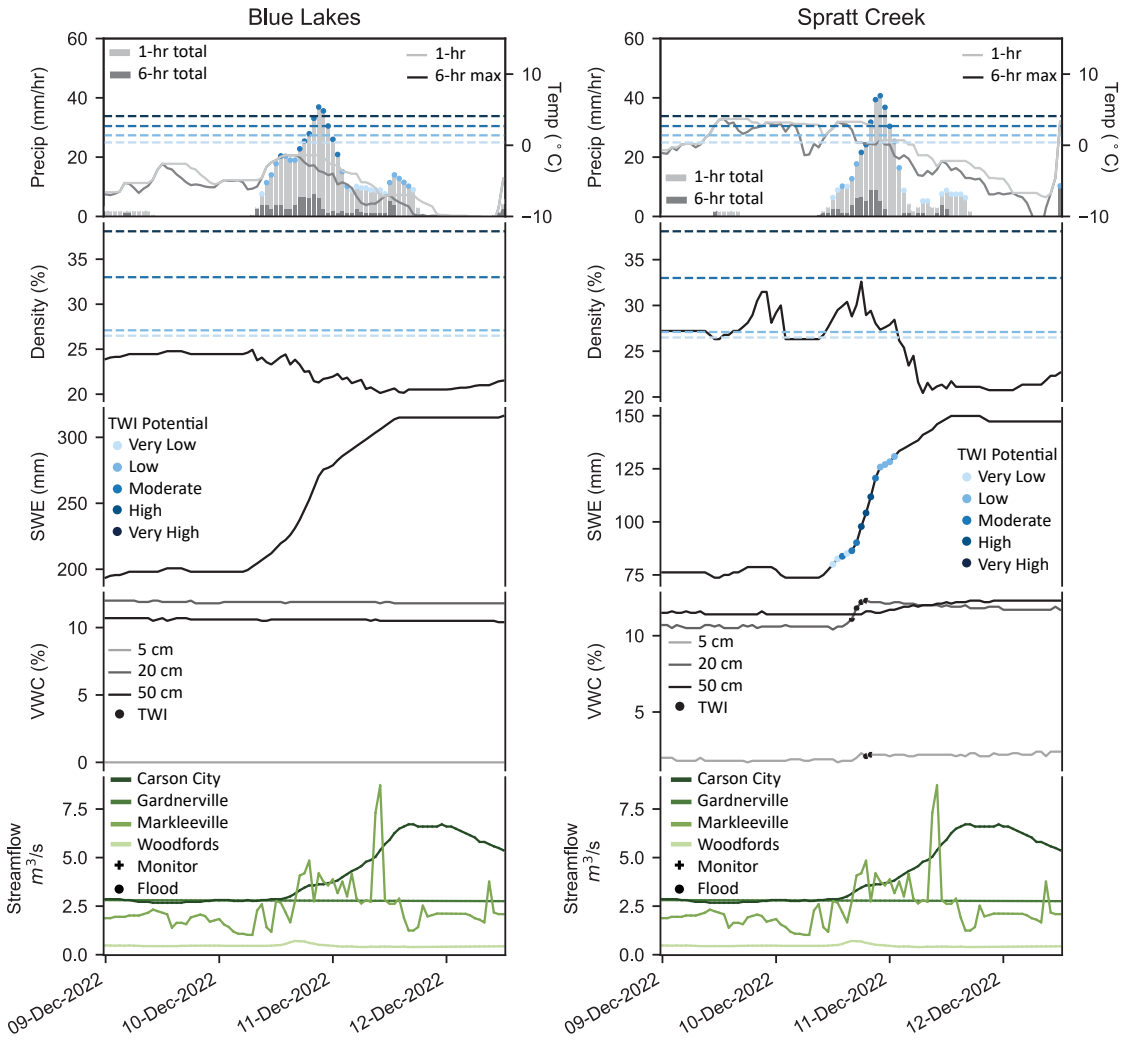

Figure A.6: SR-DSS event assessment: 9 – 12 December 2022

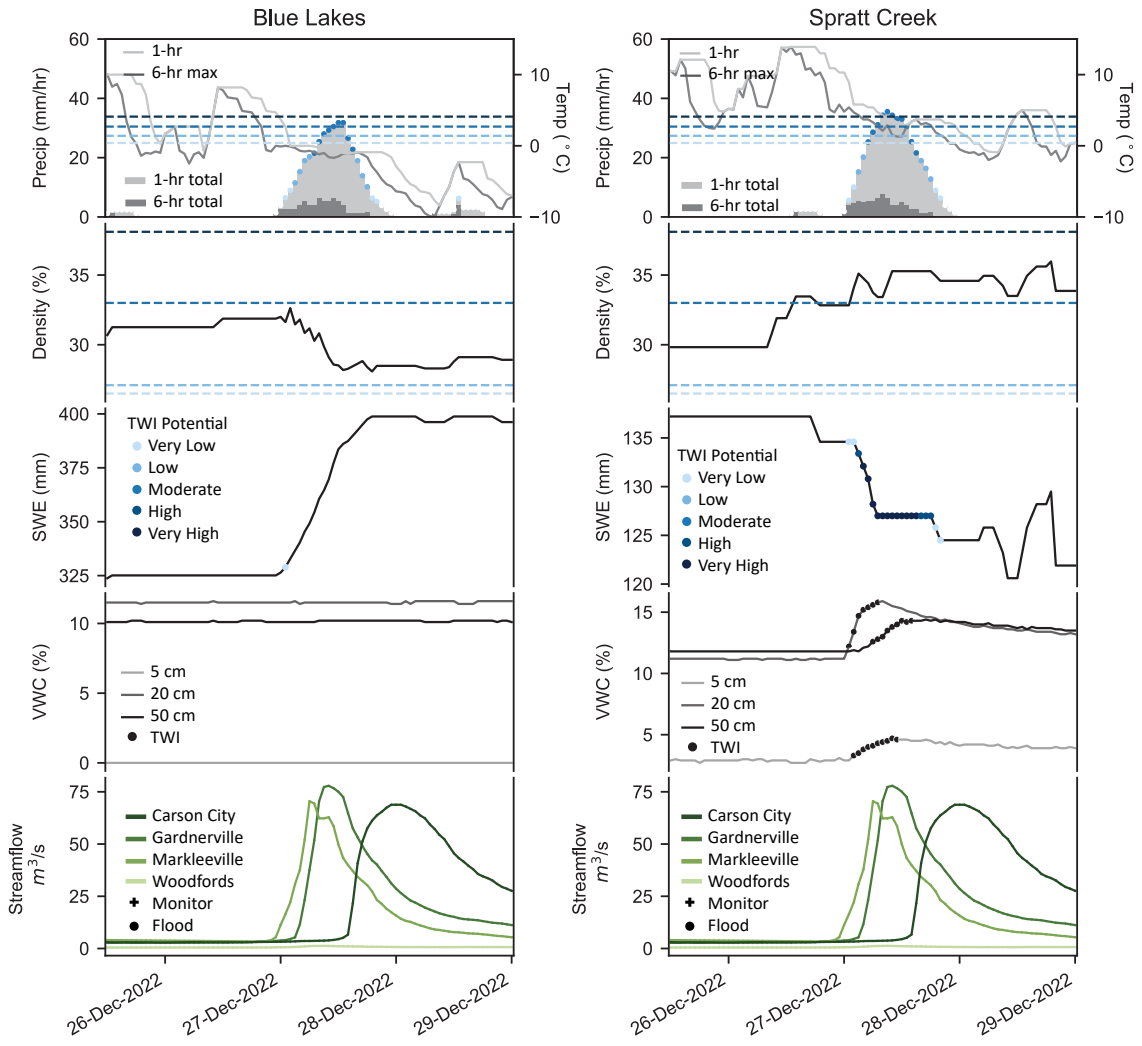

Figure A.7: SR-DSS event assessment: 26 – 28 December 2022

Appendix B

Design Tables

Table B.1: Results of six culvert designs for site #1 using a rectangular concrete section, with and without a surge factor of 1.16, an inlet treatment with Ke=0.70, and three different crest elevations.

L	Slope	Q	TW	Crest	Inlet Treatment	Barrels	Span	Rise	HW	Overtopping
20	2%	610	6.3	10	Square Edge (0° flare) Wingwall (Ke=0.7)	2	6.0	5.0	8.75	699.72
20	2%	708	6.3	10	Square Edge (0° flare) Wingwall (Ke=0.7)	2	6.0	6.0	8.66	790.78
50	2%	610	6.3	15	Square Edge (0° flare) Wingwall (Ke=0.7)	2	5.0	4.0	14.05	633.63
50	2%	708	6.3	15	Square Edge (0° flare) Wingwall (Ke=0.7)	2	5.0	5.0	13.04	776.67
200	2%	610	6.3	20	Square Edge (0° flare) Wingwall (Ke=0.7)	2	5.0	4.0	14.05	745.59
200	2%	708	6.3	20	Square Edge (0° flare) Wingwall (Ke=0.7)	2	5.0	4.0	18.21	745.59

Table B.2: Results of six culvert designs for site #1 using a rectangular concrete section, with and without a surge factor of 1.16, an inlet treatment with Ke=0.20, and three different crest elevations.

L	Slope	Q	TW	Crest	Inlet Treatment	Barrels	Span	Rise	HW	Overtopping
20	2%	610	6.3	10	1:1 Bevel (45° flare) Wingwall (Ke=0.2)	2	5.0	5.0	8.82	687.86
20	2%	708	6.3	10	1:1 Bevel (45° flare) Wingwall (Ke=0.2)	2	6.0	5.0	8.61	825.44
50	2%	610	6.3	15	1:1 Bevel (45° flare) Wingwall (Ke=0.2)	2	4.0	4.0	15.06	609.05
50	2%	708	6.3	15	1:1 Bevel (45° flare) Wingwall (Ke=0.2)	2	5.0	4.0	13.23	761.31
200	2%	610	6.3	20	1:1 Bevel (45° flare) Wingwall (Ke=0.2)	2	4.0	4.0	15.24	711.25
200	2%	708	6.3	20	1:1 Bevel (45° flare) Wingwall (Ke=0.2)	2	4.0	4.0	19.55	716.66

Table B.3: Results of six culvert designs for site #1 using a circular metal pipe section, with and without a surge factor of 1.16, an inlet treatment with Ke=0.70, and three different crest elevations.

L	Slope	Q	TW	Crest	Inlet Treatment	Barrels	D	HW	Overtopping
20	2%	610	6.3	10	Mitered to Conform to Slope (Ke=0.7)	2	6	9.63	628.73
20	2%	708	6.3	10	Mitered to Conform to Slope (Ke=0.7)	2	6.5	9.79	720.01
50	2%	610	6.3	15	Mitered to Conform to Slope (Ke=0.7)	2	5	15.02	608.37
50	2%	708	6.3	15	Mitered to Conform to Slope (Ke=0.7)	2	5.5	14.55	722.67
200	2%	610	6.3	20	Mitered to Conform to Slope (Ke=0.7)	2	5	17.97	648.38
200	2%	708	6.3	20	Mitered to Conform to Slope (Ke=0.7)	2	5.5	14.55	813.87

Table B.4: Results of six culvert designs for site #1 using a circular metal pipe section, with and without a surge factor of 1.16, an inlet treatment with Ke=0.20, and three different crest elevations.

L	Slope	Q	TW	Crest	Inlet Treatment	Barrels	D	HW	Overtopping
20	2%	610	6.3	10	Beveled Edge (1:1) (Ke=0.20)	2	5.5	9.53	636.36
20	2%	708	6.3	10	Beveled Edge (1:1) (Ke=0.20)	2	6	9.52	737.41
50	2%	610	6.3	15	Beveled Edge (1:1) (Ke=0.20)	2	5	11.81	721.3
50	2%	708	6.3	15	Beveled Edge (1:1) (Ke=0.20)	2	5	14.59	721.29
200	2%	610	6.3	20	Beveled Edge (1:1) (Ke=0.20)	2	5	16.09	691.01
200	2%	708	6.3	20	Beveled Edge (1:1) (Ke=0.20)	2	5.5	11.49	871.92

Table B.5: Results of six culvert designs for site #2 using a rectangular concrete section, with and without a surge factor of 1.16, an inlet treatment with Ke=0.70, and three different crest elevations.

L	Slope	Q	TW	Crest	Inlet Treatment	Barrels	Span	Rise	HW	Overtopping
20	2%	11.0	2	4	Square Edge (0° flare) Wingwall (Ke=0.7)	1	3.0	2.0	1.72	44.25
20	2%	12.8	2	4	Square Edge (0° flare) Wingwall (Ke=0.7)	1	–	–	–	–
50	2%	11.0	2	8	Square Edge (0° flare) Wingwall (Ke=0.7)	1	3.0	2.0	1.72	69.74
50	2%	12.8	2	8	Square Edge (0° flare) Wingwall (Ke=0.7)	1	–	–	–	–
200	2%	11.0	2	10	Square Edge (0° flare) Wingwall (Ke=0.7)	1	3.0	2.0	1.72	79.08
200	2%	12.8	2	10	Square Edge (0° flare) Wingwall (Ke=0.7)	1	–	–	–	–

Table B.6: Results of six culvert designs for site #2 using a circular concrete section, with and without a surge factor of 1.16, an inlet treatment with Ke=0.70, and three different crest elevations.

L	Slope	Q	TW	Crest	Inlet Treatment	Barrels	D	HW	Overtopping
20	2%	11.0	2	4	Mitered to Conform to Slope (Ke=0.7)	1	1.75	2.96	18.24
20	2%	12.8	2	4	Mitered to Conform to Slope (Ke=0.7)	1	–	–	–
50	2%	11.0	2	8	Mitered to Conform to Slope (Ke=0.7)	1	1.5	2.9	20.86
50	2%	12.8	2	8	Mitered to Conform to Slope (Ke=0.7)	1	–	–	–
200	2%	11.0	2	10	Mitered to Conform to Slope (Ke=0.7)	1	1.5	2.9	22.45
200	2%	12.8	2	10	Mitered to Conform to Slope (Ke=0.7)	1	–	–	–

Table B.7: Results of six culvert designs for site #2 using a circular metal pipe section, with and without a surge factor of 1.16, an inlet treatment with Ke=0.70, and three different crest elevations.

L	Slope	Q	TW	Crest	Inlet Treatment	Barrels	D	HW	Overtopping
20	2%	11.0	2	4	Mitered to Conform to Slope (Ke=0.7)	1	2.0	1.85	23.14
20	2%	12.8	2	4	Mitered to Conform to Slope (Ke=0.7)	1	–	–	–
50	2%	11.0	2	8	Mitered to Conform to Slope (Ke=0.7)	1	1.5	3.88	17.15
50	2%	12.8	2	8	Mitered to Conform to Slope (Ke=0.7)	1	–	–	–
200	2%	11.0	2	10	Mitered to Conform to Slope (Ke=0.7)	1	1.5	6.46	13.1
200	2%	12.8	2	10	Mitered to Conform to Slope (Ke=0.7)	1	–	–	–

Appendix C

Design Example

Design the culvert contained in design guideline 1 of the FHWA Hydraulic Design Manual (Schall et al., 2012) using surge factors 1, 1.05, 1.16, 1.33, and 2.15. Table B.1 shows the design results for the distinct surge factors. As indicated in rows 2-4, the culvert diameter increases for surge factors greater than 1.16 in all cases. This indicates that existing culvert designs of similar proportions in the State of Nevada may fail the overtopping criterion provided the factors outlined below were applied.

Table C.1: Results of the design provided in the FHWA hydraulic design manual (2011).

L	Slope	Surge Factor	Q	TW	Crest	Inlet Treatment	Barrels	D	HW
200	1	1.00	200	3.5	10	Beveled Edge (1:1) (Ke=0.20)	1	4.5	7.9
200	1	1.16	232	3.5	10	Beveled Edge (1:1) (Ke=0.20)	1	4.5	9.51
200	1	1.33	266	4.0	10	Beveled Edge (1:1) (Ke=0.20)	1	5.0	9.01
200	1	2.15	430	4.5	10	Beveled Edge (1:1) (Ke=0.20)	1	6.5	9.61

Bibliography

Anderson, J. and Wirt, J. (2008). Ultrasonic snow depth sensor accuracy, reliability, and performance. Hood River, OR.

ASTM (2020). ASTM A760/A760M-15 (2020): Standard Specification for Corrugated Steel Pipe, Metallic-Coated for Sewers and Drains. https://doi.org/10.1520/A0760_A0760M-15R20.

ASTM (2021). ASTM B745/B745M-15 (2021): Standard Specification for Corrugated Aluminum Pipe for Sewers and Drains. https://doi.org/10.1520/B0745_B0745M-15R21.

ASTM (2022). ASTM C76-22a: Standard Specification for Reinforced Concrete Culvert, Storm Drain, and Sewer Pipe. https://doi.org/10.1520/C0076-22.

Crameri, F., Shephard, G. E., and Heron, P. J. (2020). The misuse of colour in science communication. *Nature Communications*, 11(1).

FHWA (2022). HY-8 Culvert Hydraulic Analysis Program (7.80.2). https://www.fhwa.dot.gov/engineering/hydraulics/software/hy8/.

Gordon, A., Chimenti, E., Amirazizi, R., Busalacchi, S., Buhler, M., Goedderz, P., Grevin, C., and Kashani, S. (2022). Crafting effective public safety messages for wildfire and subsequent debris flow risks.

Hastie, T., Tibshirani, R., and Friedman, J. (2009). *The Elements of Statistical Learning: Data Mining, Inference, and Prediction*. Springer Science+Business Media, LLC.

Hatchett, B. J. (2021). Seasonal and ephemeral snowpacks of the conterminous united states. *Hydrology*, page 2020110545.

Hatchett, B. J., Benmarhnia, T., Guirguis, K., VanderMolen, K., Gershunov, A., Kerwin, H., Khlystov, A., Lambrecht, K. M., and Samburova, V. (2021). Mobility data to aid assessment of human responses to extreme environmental conditions. *The Lancet Planetary Health*, 5(10):e665–e667.

Hatchett, B. J., Cao, Q., Dawson, P. B., Ellis, C. J., Hecht, C. W., Kawzenuk, B., Lancaster, J. T., Osborne, T. C., Wilson, A. M., Anderson, M. L., Dettinger, M. D., Kalansky, J. F., Kaplan, M. L., Lettenmaier, D. P., Oakley, N. S., Ralph, F. M., Reynolds, D. W., White, A. B., Sierks, M., and Sumargo, E. (2020). Observations of an extreme atmospheric river storm with a diverse sensor network. *Earth and Space Science*, 7(8).

Hatchett, B. J., Koshkin, A. L., Guirguis, K., Rittger, K., Nolin, A. W., Heggli, A., Rhoades, A. M., East, A. E., Siirila-Woodburn, E. R., Brandt, W. T., Gershunov, A., and Haleakala, K. (2023). Midwinter dry spells amplify post-fire snowpack decline. *Geophysical Research Letters*, 50(3).

Heggli, A. (2023). *Improving Decision Support During High Impact Weather Through Data Analysis and Visual Communication*. PhD thesis, University of Nevada, Reno.

Heggli, A., Hatchett, B., Schwartz, A., Bardsley, T., and Hand, E. (2022). Toward snowpack runoff decision support. *iScience*, 25(5):104240.

Heggli, A., Hatchett, B., Tolby, Z., Lambrecht, K., Collins, M., Olman, L., and Jeglum, M. (2023). Visual communication of probabilistic information to enhance decision support. *Bulletin of the American Meteorological Society*, 104(9):E1533–E1551.

Kattlemann, R. (1997). Flooding from rain-on-snow in the Sierra Nevada. In *Destructive Water: Water-Caused Natural Disasters, Their Abatement and Control*, page 412, Anaheim, California.

McCabe, G. J., Clark, M. P., and Hay, L. E. (2007). Rain-on-snow events in the western united states. *Bulletin of the American Meteorological Society*, 88(3):319–328.

McGurk, B., Azuma, D., and Kattelmann, R. (1988). Density of new snow in the central sierra nevada. In *Proceedings 56th Western Snow Conference*, pages 71–80.

Musselman, K. N., Lehner, F., Ikeda, K., Clark, M. P., Prein, A. F., Liu, C., Barlage, M., and Rasmussen, R. (2018). Projected increases and shifts in rain-on-snow flood risk over western north america. *Nature Climate Change*, 8(9):808–812.

NACSE (2024). Prism climate data. `https://prism.oregonstate.edu/`.

National Weather Service Western Regional Headquarters (2022). Risky business - supplement for advancing idss through probabilities. Technical report.

NDOT (2006). Drainage manual, hydraulics section. `https://www.dot.nv.gov/home/showpublisheddocument/1663/636183602579530000`.

NOAA (2016). GHCN (global historical climatology network) daily documentation. `https://www1.ncdc.noaa.gov/pub/data/cdo/documentation/GHCND_documentation.pdf`.

NOAA (2024). Model analyses and guidance. `https://mag.ncep.noaa.gov/`.

NSIDC (2024). Snow data assimilation system (snodas) data products at nsidc, version 1. `https://nsidc.org/data/g02158/versions/1`.

Rhoades, A. M., Zarzycki, C. M., Inda-Diaz, H. A., Ombadi, M., Pasquier, U., Srivastava, A., Hatchett, B. J., Dennis, E., Heggli, A., McCrary, R., McGinnis, S., Rahimi-Esfarjani, S., Slinskey, E., Ullrich, P. A., Wehner, M., and Jones, A. D. (2023). Recreating the california new year's flood event of 1997 in a regionally refined earth system model. *Journal of Advances in Modeling Earth Systems*, 15(10).

Rolinski, S., Horn, H., Petzoldt, T., and Paul, L. (2007). Identifying cardinal dates in phytoplankton time series to enable the analysis of long-term trends. *Oecologia*, 153(4):997–1008.

Schall, J. D., Thompson, P. L., Zerges, S. M., Kilgore, R. T., and Morris, J. L. (2012). *Publication No. FHWA-HIF-12-026: Hydraulic design of highway culverts.*

Schneider, L. (2023). rsnodas. `https://github.com/lschneider93/rsnodas`.

Seaber, P. R., Kapinos, F. P., and Knapp, G. L. (1987). *Hydrologic unit maps: US Geological Survey water supply paper 2294*. US Geological Survey.

Siirila-Woodburn, E., Rhoades, A. M., Hatchett, B. J., Huning, L., Szinai, J., Tague, C., Nico, P. S., Feldman, D., Jones, A. D., Collins, W. D., and Kaatz, L. (2021). A low-to-no snow future and its impacts on water resources in the western United States. *Nature Reviews Earth and Environment*, 2:800–819.

Siirila-Woodburn, E. R., Dennedy-Frank, P. J., Rhoades, A., Vahmani, P., Maina, F., Hatchett, B., Zhou, Y., and Jones, A. (2023). The role of atmospheric rivers on groundwater: Lessons learned from an extreme wet year. *Water Resources Research*, 59(6):e2022WR033061. e2022WR033061 2022WR033061.

Thomas, K. A. and Williams, R. P. (1997). Flood of january 1997 in the carson river basin, california and nevada.

Uccellini, L. W. and Ten Hoeve, J. E. (2019). Evolving the national weather service to build a weather-ready nation. *Bulletin of the American Meteorological Society*, 100(10):1923–1942.

USACE (2013). Truckee meadows flood control project, nevada.

USDA (2024). Snow water equivalent (swe) — its importance in the northwest. `https://www.climatehubs.usda.gov/hubs/northwest/topic/snow-water-equivalent-swe-its-importance-northwest#`.

USGS (2018). Usgs working to restore streamgages. *USGS: Science for a Changing World*.

USGS (2022). National hydrography dataset (ver. usgs national hydrography dataset best resolution (nhd) for hydrologic unit (hu) 4 - 2001 (published 20191002).

USGS (2023). Surface-water daily data for the nation. `https://waterdata.usgs.gov/nwis/dv/?referred_module=sw`.

USGS (2024a). The national map downloader. `https://apps.nationalmap.gov/downloader/`.

USGS (2024b). Sometimes the usgs real-time stage data seems too high (or too low). are the usgs data inaccurate? `https://www.usgs.gov/faqs/sometimes-usgs-real-time-stage-data-seems-too-high-or-too-low-are-usgs-data-inaccurate`.

Wendelberger, J. G. (1982). *Smoothing noisy data with multidimensional splines and generalized cross-validation*. The University of Wisconsin-Madison.

Wilms, L. and Oberfeld, D. (2017). Color and emotion: effects of hue, saturation, and brightness. *Psychological Research*, 82(5):896–914.

Wood, S. N. (2003). Thin plate regression splines. *Journal of the Royal Statistical Society Series B: Statistical Methodology*, 65(1):95–114.

Nevada Department of Transportation

Tracy Larkin-Thomason, P.E. Director

Lucy Koury, Research Division Chief

(775) 888-7223

lkoury@dot.nv.gov

1263 South Stewart Street

Carson City, Nevada 89712